Mesoscale modelling of triaxial concrete fracture: The role of aggregate shapes

Qingchen Liu [a], Deheng Wei [a,b], Yixiang Gan [a,*]

[a] School of Civil Engineering, The University of Sydney, NSW 2006, Australia
[b] Key Laboratory of Ministry of Education on Safe Mining of Deep Mines, School of Resources and Civil Engineering, Northeastern University, Shenyang 110819, China

ARTICLE INFO

ABSTRACT

Effects of aggregate shape have become one of the research focuses on mesoscale concrete fracture. Most relevant findings are achieved from simple uniaxial tests without considering the more complex and realistic stress sustained by filed-scale engineering structures. To this end, mesoscale modelling using the finite element method (FEM) is conducted to investigate the three-phase concrete fracture behaviour subjected to triaxial compression with the presence of confining pressure. The realistic aggregate shape, characterised by the fractal dimension, is generated to emphasise the effects of aggregate morphology on the concrete strength under varying confining pressures. Quantitative evidence from a microscopic perspective on local stress, damage evolution, and crack patterns is provided to support macroscopic observations. As a result, similar to uniaxial tests, rougher aggregate with the higher fractal dimension leads to greater compressive strength of concrete. With increasing confining pressure, this effect can be amplified. We further find that the data for uniaxial-strength-normalised triaxial strength and confining pressure of concrete specimens with various aggregate shapes are well-calibrated with experimental results and can collapse onto a single universal curve. As microscopic evidence shows, the heterogeneity of stress distribution for aggregate shapes, which deviates from each other at initial loading, finally converges. Local damage exhibits a universal competition between the ITZ and aggregates, with increasing fractal dimension of aggregates, under varying confining pressures, and explains the occurrence of the scaling law in the relationship between triaxial compressive strength and confining pressure. The same competition extends to macro-cracks and is reflected in crack volume (or area) and cluster size. This study presents a pioneering effort in systematic mesoscale modelling under triaxial loading, shedding new light on the effects of the aggregate shape on the strength of concrete-like composites.

Notation

$\Omega \subset R^3$	3D domain space
VT_i	i th Voronoi cell
S_i	i th seed for i th Voronoi cell
Q	Energy functional
ρ_{vt}	Density function over Ω for the Voronoi tessellation
C_i	Mass centroid of i th Voronoi cell
N_l	Number of Lloyd iterations
H	Hurst coefficient
F_d	Fractal dimension
F_n	n th Fourier descriptor
R_r	Relative roughness
L	Side length of cubic concrete specimen (mm)
L_{vt}	Side length of cubic space for Voronoi tessellation (mm)
SF_a	Solid fraction of aggregates in concrete

(continued on next column)

(continued)

d_a	Aggregate size (mm)
ρ	Density (kg/m^3)
E	Young's modulus (MPa)
ν	Poisson's ratio
σ_c	Compressive stress (MPa)
σ_{c0}	Yield stress in compression (MPa)
σ_{cu}	Ultimate strength in compression (MPa)
σ_t	Tensile stress (MPa)
σ_{t0}	Ultimate strength in tension (MPa)
ε_c	Compressive strain
ε_{cu}	Compressive strain at σ_{cu}
ε_t	Tensile strain
ε_{t0}	Tensile strain at σ_{t0}
$\tilde{\varepsilon}_c^{pl}, \tilde{\varepsilon}_t^{pl}$	Equivalent plastic strain tensor in compression and tension

(continued on next page)

(*continued*)

$\tilde{\varepsilon}_c^{in}$	Inelastic strain in compression
$\tilde{\varepsilon}_t^{ck}$	Cracking strain in tension
a_a, a_d, α_t	Parameters in GB50010-2010
d_c, d_t	Damage variables for tension and compression in concrete damage plasticity (CDP)
t	Traction (MPa)
t_n, t_s, t_t	Current traction in normal and two shear directions (MPa)
t_0	Cohesive strength (MPa)
t_{n0}, t_{s0}, t_{t0}	Cohesive strengths in normal and two shear directions (MPa)
$\overline{t_n}, \overline{t_s}, \overline{t_t}$	Traction calculated based on the elastic-displacement behaviour for the current separations without damage in normal and two shear directions (MPa)
δ	Separation (m)
δ_f	Failure separation (m)
$\delta_n, \delta_s, \delta_t$	Separation in normal and two shear directions (m)
δ_m	Effective relative displacement (m)
δ_{m0}, δ_{mf}	Effective relative displacement at damage initiation and failure (m)
G_f	Fracture energy (N/m)
$G_{f,n}, G_{f,s}, G_{f,t}$	Fracture energy in normal and two shear directions (N/m)
k_n, k_s, k_t	Current cohesive stiffness in normal and two shear directions (N/m^3)
k_{n0}, k_{s0}, k_{t0}	Initial cohesive stiffness in normal and two shear directions (N/m^3)
d_{CIE}	Damage variable for the cohesive element
F	Sum of nodal reaction force on the top boundary (N)
A	Area of initial specimen cross-section (mm^2)
$f_{c,0}$	Uniaxial concrete strength (MPa)
σ_1	Axial stress in the loading direction (MPa)
σ_2, σ_3	Lateral stress (MPa)
σ_L	Confining pressure (MPa)
$\sigma_{1,s}$	Triaxial strength of concrete (MPa)
σ_{pe}	Mean stress of element for the mortar (MPa)
σ_{npe}	Normalised mean stress of element for the mortar
ε_1	Axial strain in the loading direction
$\varepsilon_2, \varepsilon_3$	Lateral strain
k	Fitting parameter of Eq. (23)
V_c	Volume of the cubic concrete specimen (mm^3)
V_i	Volume of i th solid element (mm^3)
$V_{pe,j}$	Volume (mm^3) of the element of mortar having $\sigma_{p,i}/\sigma_p$ within j th bin of σ_{npe}
$V_{tf,m}, S_{tf,ITZ}, V_{tf,a}$	Volume (mm^3) or area (mm^2) of cracked mortar, ITZ and aggregate
$V_{ntf,m}, S_{ntf,ITZ}, V_{ntf,a}$	Normalised value of $V_{tf,m}, S_{tf,ITZ}, V_{tf,a}$
$V_{f,m}, S_{f,ITZ}, V_{f,a}$	Volume (mm^3) or area (mm^2) of the cluster of mortar, ITZ and aggregate
$V_{nf,m}, S_{nf,ITZ}, V_{nf,a}$	Normalised value of $V_{f,m}, S_{f,ITZ}, V_{f,a}$
S_i	Area (mm^2) of i th cohesive element for ITZ
S_c	Surface area (mm^2) of cubic concrete specimen
E_i	i th element for crack
T_E	The set of elements for the crack of each material phase of concrete
$T_{E,sub,k}$	The set of elements belonging the same crack cluster
C_T	The set of separate crack clusters in each material phase
d_i	Damage of i th element for the mortar, ITZ or aggregate
D_m, D_{ITZ}, D_a	Damage of mortar, ITZ and aggregate
$D_{m,p}, D_{ITZ,p}, D_{a,p}$	Damage of mortar, ITZ and aggregate at the compressive strength of concrete
K_{npe}	Kurtosis of σ_{npe}
S_{npe}	Skewness of σ_{npe}
$f_{ln}(x_s)$	Lognormal fitting of the PDF for the random variable x_s
μ_s, σ_s	Lognormal fitting parameters
M_m, M_{ITZ}, M_a	Mean value of lognormal fitting of PDF for $V_{nf,m}, S_{nf,ITZ}, V_{nf,a}$
M_{npe}	Mean value of σ_{npe}
SD_{npe}	Standard deviation of σ_{npe}
SD_{d_a}	Standard deviation of aggregate size (mm)

1. Introduction

As a typical example of the matrix-inclusion composites containing hard particulates, concrete has emergent characteristics different from its components. Concrete industries have a worldwide consumption of about 17 billion metric tonnes per year [1]. Due to the presence of mismatched mechanical behaviour with the material constituents, one of the fundamental challenges is to quantitatively relate the microscale information to the emergent macroscopic properties [2]. It is well acknowledged that representing concrete as a homogenous material, with the advancement and development of non-local theory [3] and strain gradient models [4], has made significant progress. Nevertheless, the spatial heterogeneity is hard to be captured by such kind of mean-field approximations. The quasi-brittle behaviour of concrete is strongly influenced by the heterogeneity of its material constituents and interactions manifested over a large range of length scales [5]: from nano- to meso-scale, namely nanometre (hydrated cement paste [6]) to centimetre (the largest aggregate scale [7]). Zaitsev and Wittmann [8] conduct pioneering study on concrete as a hierarchical structure with various length scales of inhomogeneities. The primary inhomogeneity of concrete is found at the mesoscale, which has been widely treated as the most sought-after scale to focus on the influence of heterogeneity on macro mechanical response [9]. At such a scale, besides voids, concrete is composed of three phases, namely mortar matrix, coarse aggregates, and interfacial transition zone (ITZ) jointed the two phases. Even under uniform loading conditions, the heterogenous internal stress field could be encountered, resulting in severe stress concentrations, which are of high possibility to cause crack initiation at the weakest phase—ITZ [10]. Note that the multi-scale approach dedicated to the collective mechanical response can also be realised by upscaling the underlying mesoscale information as a constitutive law to the macroscopic scale to minimise the phenomenological assumptions and fitting parameters.

For experiments, a significant portion of the fundamental understanding of concrete fracture behaviour is derived from the results of simple uniaxial tests [11]. However, uniaxial tests fail to reflect the real mechanical responses of concrete structures subjected to complex multiaxial stress conditions. Although replicating the real stress conditions of concrete in experimental studies is challenging, some progress has still been made in the study of triaxial fracture of concrete [12]. As a rock-like material, some empirical failure criterions or stress-strain relations (such as the Mohr-Coulomb criterion), inspired by rock mechanics, are developed to predict the peak compressive stress of concrete; among them, three categories of stress-strain curves can be summarised: proper rational fraction, improper rational fraction, and polynomial equations [13]. Similar to the famous Hoek-Brown criterion [14,15] in rock mechanics community, in conventional triaxial tests on cylindrical concrete domain, influences of σ_2 on compressive strength cannot be specifically included, with σ_1, σ_2, and σ_3 being principal stresses and $\sigma_1 > \sigma_2 = \sigma_3$. Meanwhile, the true triaxial compression tests, that are closer to real concrete stress conditions with the macro stress anisotropy, $\sigma_1 > \sigma_2 > \sigma_3$, are of higher priority when morphology anisotropy comes into play. Bridging length scales, a few studies have highlighted the influence of mesoscale heterogeneity in concrete on macroscopic failure criterion, with a particular focus on aggregate type (e.g., natural and recycled aggregates) [16] and aggregate morphology [17]. However, there is insufficient evidence to support the changes in the microscale localisation and failure mechanisms within the concrete due to differences in aggregate properties. For this concern, one of studies employs X-ray computed tomography (CT) combining with in situ tests to identify the strain localisation and crack network development within local regions (e.g., mortar, aggregate and pore) of concrete under triaxial stress conditions [38]. However, none of the tests consider the effects of aggregate shape, when local damage and failure of concrete are investigated under uniaxial or triaxial stress conditions. From the overview of experiments, conducting the refined study on the effects of aggregate shape and eliminating disturbance of other factors remain challenging. Additionally, achieving a controlled variation in the shape irregularity of aggregate is also difficult. Considering the above concerns, the effects of aggregate shape on the underlying micro-mechanics rooted in grain-scale heterogeneity remains to be emphasised, in order to clarify the rigorousness and validity of macroscopic findings.

Mesoscale simulations have been proven as an effective alternative to experimental approaches to reveal the influences of local

heterogeneities on the complex global response [8]. Up to now, mesoscale studies on concrete fracture behaviour can be classified into three categories, namely the finite element method (FEM) in the context of continuum mechanics, the discrete element method (DEM) and the combination of such two methods. Due to the maturity and rigorousness of continuum mechanics, many continuum-fashion mesoscale models have been proposed, such as the truss model [18] and the lattice model [19]. Considering that substantial cracks could initiate, grow, and coalesce and much more input energy is consumed by frictional contacts at these cracks than the newly created fractures themselves [20], accurate simulations of fracture evolutions in concrete require careful considerations of a large number of discrete contacts. Since then, DEM featured with contact searching and determining becomes popular in concrete-like-composite crack modelling; cracks are enriched in the bonds between connected elementary spheres in 3D (or circles in 2D) DEM. However, many physically meaningless local parameters in DEM parallel bond models are required to be fitted. The primary bulk elasticity, in terms of Young's modulus and Poisson's ratios, is highly dependent on element packing structures; albeit the same calibrated parameters are utilised, the elasticity can no longer be warranted [21] when the packing structure is alternated. The combined finite and discrete element method (FDEM) [22], importing the capability of DEM to handle contacts to explicit FEM framework with crack initiations and evolutions, fits within the context of the accurately simulating fracture behaviour of mesoscale concretes.

Mesoscale concrete models often require topological reconstructions of different material phases. The bottom-up method—a dense or loose random packing of artificially shaped and sized aggregates with mortar matrix filling the space between them—may be the most popular among others [23]. Due to the resulting loose packing structure, the target solid fraction of aggregates is typically achieved by mechanical compressions, such as the die compaction, which could induce strong strain localisations or even shear bands within the domain, hindering the investigation of heterogeneity-influenced concrete fracture behaviour with the natural adequacy. By contrast, during the real concreting process, coarse aggregates are homogenously suspended within the mortar phase, with less variances in local aggregate fractions. Moreover, aggregate shapes utilised in most of such bottom-up methods are simple convex shapes (e. g., spheres, polyhedrons and ellipsoids) [24]. Natural grains have fractal-like shapes with higher irregularities on their surfaces, where more stress concentrations can be induced on the joints between the mortar and the aggregate phases. In recent years, with the development of non-destructive 3D imaging techniques (including magnetic resonance imaging (MRI), and X-Ray and neutron tomography), real meso-morphologies became accessible. It has to be mentioned that *in situ* [25] and *ex situ* [26] X-Ray mechanical tests are also conducted on quasi-static localised deformation on mesh-scale concrete. However, unavoidable, yet large creep strains are encountered in the small-scale concrete specimen due to the long durations required form imaging towards full 3D spatial evolutions. Although the scanned 3D heterogeneity of concretes with packed aggregates can be readily imported into numerical models, the subsequent mechanical analysis is highly sensitive to the randomly packing structure [24]. Consequently, the numerical method seems to be a plausible alternative to isolate effects of heterogeneity rooted in aggregate morphology on concrete strength from other dominant factors. Another type of method in numerically modelled mesoscale heterogeneity is based on the top-down fashion. In these methods, global descriptors, such as aggregate fraction, specific formulations of the two-point correlation function, and more microscale statistical information extracted from the real 3D images, are realised by randomised processes [27]. Before the net homogenous distribution of aggregates is ready, unphysical, although hard to determine, features must be removed [28], followed by separating or labelling single aggregates from the whole solid phase. These steps could bring additional uncertainties in these aggregate shapes, such as their sizes, and even the aggregate grading cannot be exactly sustained as the target distribution,

as the first mesoscale factor to determine the concrete strength [29]. To capture realistic heterogeneously-localised deformations of mesoscale concrete specimens, an explicit method must be proposed to account for both the homogenously packing structures of aggregates and the high-fidelity aggregate morphology features.

For the mesoscale modelling of concrete fracture, the inherent heterogeneity of the mesoscale structure can be characterised by assigning distinct material properties to the mortar, aggregate, and interfacial transition zone (ITZ) phases [30–33]. This is based on constitutive laws implemented in various numerical models, such as the CDP model [34, 35], cohesive element method [36,37], Johnson–Holmquist Concrete (JHC) model [38,39] and others [40]. Interestingly, a novel combination of numerical models has been adopted in some studies, where the CDP model is used for the solid elements of mortar and aggregates, while zero-thickness cohesive elements considering the ratio of shear to normal strength are applied to represent the ITZ phase [41,42]. Given appropriate material properties for each material phase, mesoscale models can effectively capture the stress–strain response of concrete and have been widely used to investigate fracturing processes under various stress conditions, including static [36,43,44], dynamic [43,45,46], uniaxial [36,37,47,48] and multiaxial [43,45,49] loadings. The 3D mesoscale structures of concrete in these studies are generated using either scan-dependent (i.e., X-ray computed tomography) or scan-independent approaches (i.e., computer-based packing algorithms). The influence of material properties or the morphology of material constituents, such as the ITZ [50,51], aggregates [50,52], and pores [24], on concrete fracture has been extensively studied. Although digital imaging allows the mesoscale structure to capture greater heterogeneity in concrete, including pores in the mortar phase, which significantly affect the formation of crack networks [23,53,54], few studies focus on the influence of aggregate shape. This is more commonly explored using the latter approach, such as the take-in-place method [41,42,48,55], random extension method [56–58], and Voronoi-tessellation-based method [22,59–62], which generate particle packings through computer programming.

Some studies have highlighted the effects of aggregate shape on concrete strength [22,24,35,36], local damage mechanisms [22,24], and failure patterns [24,35,36]. For instance, compared to cases with spherical aggregates, Wei et al. concluded that more concave and irregular aggregate shapes can induce higher stress concentrations and enhance the compressive strength of concrete. Moreover, this study quantitatively analysed the relationship between local damage and concrete strength, showing that with more concave aggregate shapes, cracking tends to occur more within the aggregates and less in the ITZ [22]. On another note, although some studies have compared the failure patterns of concrete with different aggregate shapes, these comparisons often rely heavily on visual observations and lack quantitative evidence [35,36]. While stress distribution in the host matrix is used as an indicator of the fracture behaviour of heterogeneous materials [63], it has not yet been applied to analyse the influence of aggregate shape. Looking at existing literature on mesoscale studies on the influence of aggregate morphology, most are only dedicated to uniaxial compression or tension. Although some numerical progress has been made in investigating the triaxial failure of concrete, these efforts have primarily focused on stress-strain responses [45,64], without incorporating realistic aggregate shapes in concrete models. Moreover, assessing the effect of aggregate shape only based on macroscopic responses is insufficient. It is essential to support such assessments with comprehensive and quantitative analysis of the local responses of concrete at the microscopic level. However, such investigations under triaxial loading conditions are still lacking.

Based on the above discussions, in this study, we conduct mesoscale FEM modelling on triaxial compression induced fracture behaviour of three-phase concretes. The aggregates are generated with realistic shapes and are assumed to be distributed in a homogeneous mortar, without considering the influence of pores. The effect of aggregate shape

on concrete strength under triaxial loading is investigated. We aim to enrich the understanding of this effect, with a focus on local responses, including stress distributions, local damage, and crack patterns, which may provide insights into variations in macroscopic strength. The reminder of this paper is structured as follows. In Section 2, the packing/parking process is firstly introduced for the 3D mesoscale concrete structure containing the irregularly shaped aggregates; with the target size distribution in hand, their positions and orientations are inherited from the Voronoi tessellation of the domain, while specific morphology features are realised by the combined method of random field and Fast Fourier Transformation. The FEM mesh generation and constitutive models, including the damage laws for cohesive interface elements of ITZ and concrete damage plasticity (CDP) of both aggregate and mortar elements, are also provided. Section 3 validates our numerical results by comparing them with some existing experimental results, and then demonstrates the macroscopic stress-strain curves under both uniaxial and triaxial compression loading conditions. The universality of aggregate-shape-influenced triaxial strength is analysed in Section 4 by quantitative statistics of microscopic stress distributions, evolutions of local damages, and crack patterns. Main conclusions are finally summarised in Section 5.

2. Methodology

In this section, the mesoscale modelling of concrete fracture under the triaxial stress condition is conducted in two stages. Mesoscale structures with irregularly shaped aggregates are generated to represent the cubic concrete specimen in Section 2.1. For the packing algorithm, the Voronoi tessellation as well as generation of fractally shaped aggregates within a predefined cubic space are illustrated in Section 2.1.1 and 2.1.2, respectively. The construction of the mesoscale structure of a three-phase cubic concrete specimen, including mortar, ITZ and aggregate, is then provided in Section 2.1.3. Section 2.2 introduces the constitutive laws for mesoscale structure of concrete including the CDP for mortar and aggregate in Section 2.2.1 and cohesive element method for ITZ in Section 2.2.2, which are employed for the finite element modelling. In Section 2.3, boundary conditions for simulating the quasi-static triaxial tests are described.

2.1. Mesoscale structure of concrete

The effects of aggregate shape under triaxial stress conditions are investigated using a cubic concrete specimen, where the aggregates are assumed to be non-contacting and fully contained within the specimen domain. The key to generate the mesoscale structure is to produce initial
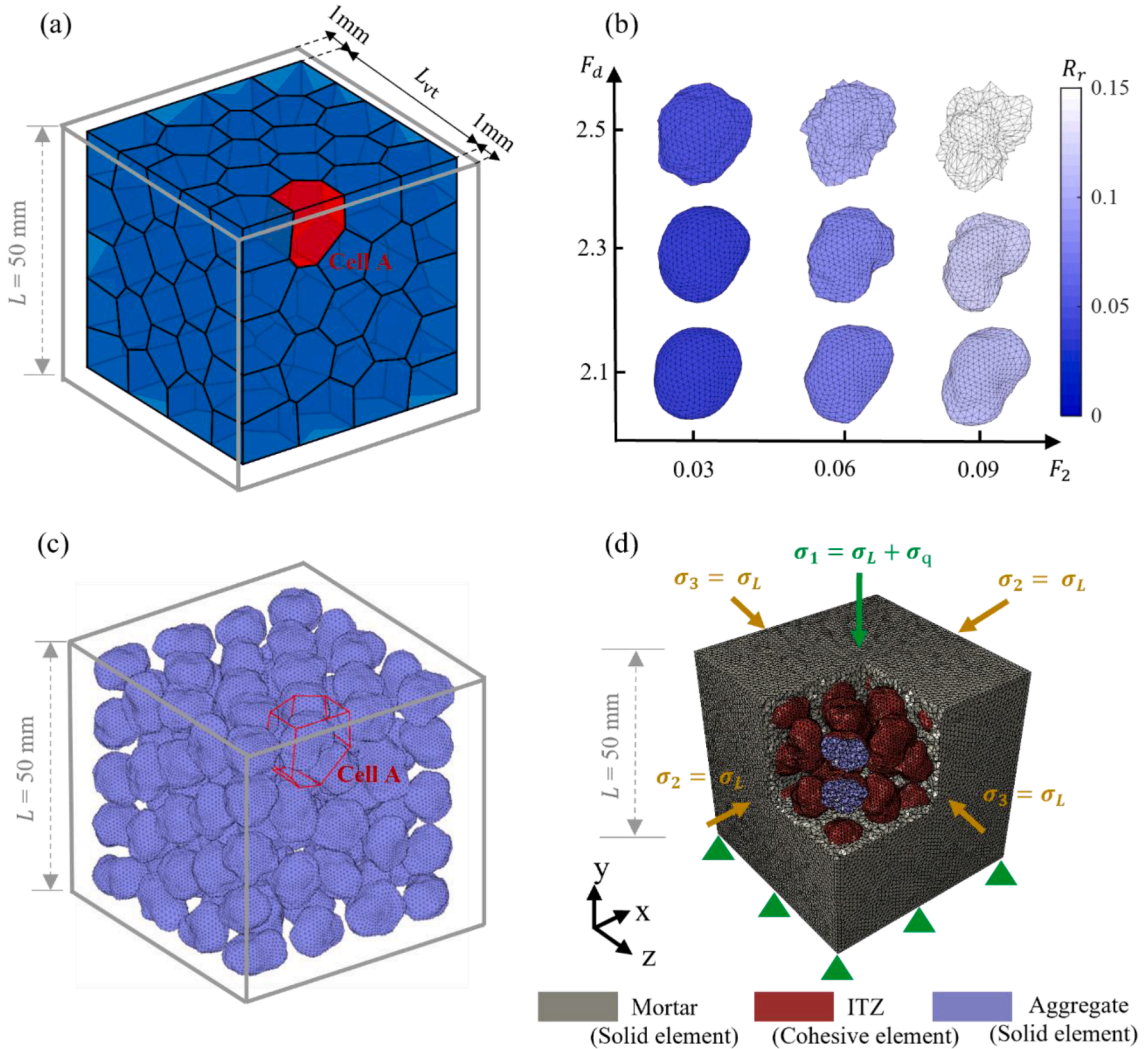

Fig. 1. (a) A typical Voronoi tessellation, (b) irregular aggregate shapes varying with fractal dimension, F_d, and the normalised second Fourier descriptor, F_2, in Cell A of (a), of which the colour bar is used to denote the relative roughness, R_r, (c) packing of irregularly shaped aggregates corresponding to the Voronoi tessellation in (a), and (d) schematic diagram of finite element (FE) modelling of the triaxial test, with arrows indicating the directions of the principal stresses of σ_1, σ_2 and σ_3.

aggregation packing within a reasonable range of packing density. To handle the packing problem of realistic shaped aggregates beyond idealised convex shapes, we have referred to the work of Mollon and Zhao [65]. A specific cubic space can be divided into Voronoi cells. Then, the irregular aggregate shape characterised by the fractal dimension, F_d, is generated fully inside each Voronoi cell. By such packing processes, any contact or overlapping can be avoided. As shown in Fig. 1(a-c), when the aggregate shapes are varied within the same Voronoi cell, the spatial distribution and orientation, which are factors affecting the mechanical performance of heterogeneous materials [63,66], are kept the same for the generated shape. This can refine the investigation into the effects of aggregate shape. Mesoscale structures of concrete are typically generated in accordance with the Fuller curve to achieve a more realistic aggregate grading, which has been shown to significantly affect concrete strength, particularly with regard to the effects of maximum aggregate size [67,68]. To minimise interference from such effects in this study, nearly mono-sized aggregates are assumed in the concrete specimens to maintain consistent grading across different aggregate shapes, while still preserving the main heterogeneity of concrete. Although these assumptions allow us to control only the aggregate shape, they lead to a simplified mesoscale structure that does not fully represent real concrete. This is a limitation that will be addressed in future work by incorporating aggregate characteristics under more realistic conditions.

2.1.1. Voronoi tessellation

In the 3D domain space $\Omega \subset R^3$, a Voronoi tessellation $\{VT_i\}_{i=1}^M$ is a partition of Ω into M regions close to a set of seeds $\{S_i\}_{i=1}^M \subset \Omega$, if $VT_i \cap VT_j = \varnothing$ for $i \neq j$ and $\cup_{i=1}^M VT_i = \Omega$. Each Voronoi cell VT_i corresponding to the seed S_i is defined in Eq. (1) [69]. The Voronoi cell VT_i consisted of every point x in the region:

$$VT_i = \left\{ x \in \Omega, \ ||x - S_i|| \leq ||x - S_j||, \ \text{for } j > 1, \ j \neq i \right\}, \tag{1}$$

where $|| \cdot ||$ denotes a Euclidean distance in R^3. The energy functional associated to sets of $\{VT_i\}_{i=1}^M$ and $\{S_i\}_{i=1}^M$ is used to introduce the differences of Voronoi cell geometry [69]:

$$Q\left(\{S_i\}_{i=1}^M, \ \{VT_i\}_{i=1}^M\right) = \sum_{i=1}^M \int_{VT_i} \rho_{vt}(x)||x - S_i|| \ dx, \tag{2}$$

where $\rho_{vt}(x)$ is a density function over a domain. Clearly, the Q is minimised only if Voronoi tessellation has the seed S_i coincided with the mass centroid of Voronoi cell $C_i = \int_{VT_i} x \rho_{vt}(x)dx / \int_{VT_i} \rho_{vt}(x)dx$ (i.e., Centroid Voronoi tessellation). Meanwhile, the Voronoi cell geometry becomes the most stable. Arbitrarily chosen seeds are usually not the mass centroids of their associated Voronoi cells, and reaching the coincidence is very difficult. The Lloyd iteration is used in this study to minimise Q by alternately moving the seed to the mass centroid of the Voronoi cell [70]. The number of Lloyd iterations N_l is a key factor to control the aggregate size and will be determined with the appropriate value later.

2.1.2. Packing for irregular aggregate shapes

In the 3D case, the existing method (i.e., a combination of the random field and Fourier-shape-descriptor based method) from the work of Mollon and Zhao [65], is employed to generate the irregularly shaped aggregate inside each Voronoi cell. In the current paper, based on the codes (MATLAB program accessible via http://guilhem.mollon. free.fr), we have improved this method by introducing the fractal dimension, F_d, which is a multiscale geometric index to characterise the aggregate shape. For the Fourier descriptor, F_n, the F_0 is normally set to 1 for the normalisation, $F_1 = 0$ ensures that the aggregate centroid has been properly chosen. F_2, F_n for $3 \leq n < 8$ and $n \geq 8$ are used to control the elongation, irregularity and surface roughness of aggregate particles, respectively. For the natural aggregate, F_n for $n \geq 2$ has a roughly linear decrease with the n in the log-log scale. According to Wei et al. [71], the

exponential relation between F_n and n can be described using the Hurst coefficient, H, which is associated with fractal dimension, F_d, as follows:

$$F_n \propto n^{-2H}, \tag{3}$$

$$F_d = 3 - H, \tag{4}$$

where $-2H$ is the slope of relation between $\log(F_n)$ and $\log(n)$. Thus, F_n can be controlled by F_d and F_2, as below [71]:

$$F_n = F_2 \left(\frac{n}{2}\right)^{2F_d - 6}. \tag{5}$$

The relative roughness, R_r, can be used to compute how globally different the irregular aggregate shape is from r_0, the mean radial length [22], as below:

$$R_r = \sqrt{\sum_{n=2}^{\infty} \left(F_2 \left(\frac{n}{2}\right)^{2F_d - 6} \right)^2}. \tag{6}$$

Given an example of Voronoi cells (i.e., Cell A) in Fig. 1(a), Fig. 1(b) shows the aggregate shapes generated at different combinations of F_d and F_2, and we can see higher values of F_d and F_2 causing the aggregate shape with the rougher surface. The size scaling of aggregate from its mass centre is required to not only reach the given packing density but also ensure the aggregate particle completely located inside the respective Voronoi cell. Consequently, any contact or overlapping between aggregate boundaries can be avoided. Then, the packing for irregularly shaped aggregates characterised by the fractal dimension is completed and used to produce the mesoscale structure for the concrete specimen in the following.

2.1.3. Generation of material components for the mesoscale model

The cubic concrete specimen with the side length of L is used for the modelling of triaxial tests. To prevent aggregate boundaries from contacting with the borders of concrete specimen, the cubic space for the Voronoi tessellation has the side length of L_{vt} is slightly smaller than L as in Fig. 1(a). Then, if the target solid fraction of aggregate is SF_a, the packing density is required to reach the $SF_a(L/L_{vt})^3$. For this study, all the mesoscale structures for concrete specimen are constructed with $L = 50$mm. In some mesoscale models of concrete [35,36,72–74], the aggregate solid fraction often reaches a certain high value exceeding 35 %. It is challenging to isolate the influence of a single aggregate characteristic from others. To conduct a refined investigation, the effects of aggregate shape are investigated under a relatively low solid fraction (at 30 %), allowing variation of aggregate shape without any overlaps between aggregates. In the virtual samples, the solid fraction, size distribution, and spatial distribution are kept the same across different shapes to emphasis on the effects of aggregate morphology. As mentioned in Naderi et al. [35], L needs to be guaranteed at least three to five times of the maximum aggregate size to be representative. To satisfy this condition and keep $SF_a = 30$ %, our concrete specimen is designed to contain 105 aggregates, as illustrated in Fig. 1(c). Here, we have defined the aggregate size d_a as the volume-equivalent sphere diameter to within a concrete specimen. Based on the standard deviation of d_a, SD_{d_a}, the effects of the number of Lloyd iterations, N_l, on d_a is investigated, when various aggregate shapes are considered for the mesoscale structure of concrete specimen. As shown in Fig. 2(a), an increase in N_l leads to a decrease in SD_{d_a} and a more uniform aggregate size distribution. To minimise fluctuations in aggregate size within the concrete specimen, $N_l = 50$ is decided for the Voronoi tessellation. For different aggregate shapes, this results in similar size grading curves as shown in Fig. 2(b), with d_a mostly varying from around 8 to 9 mm, closely approximating a mono-sized aggregate. Thus, the influence of aggregate size distribution can be minimised in this study.

Given the Voronoi tessellation with 105 seeds and 50 Lloyd iterations as shown in Fig. 1(a), an example of packing of irregularly shaped aggregates with $F_d = 2.3$ and $F_2 = 0.06$ as in Fig. 1(c) is made for
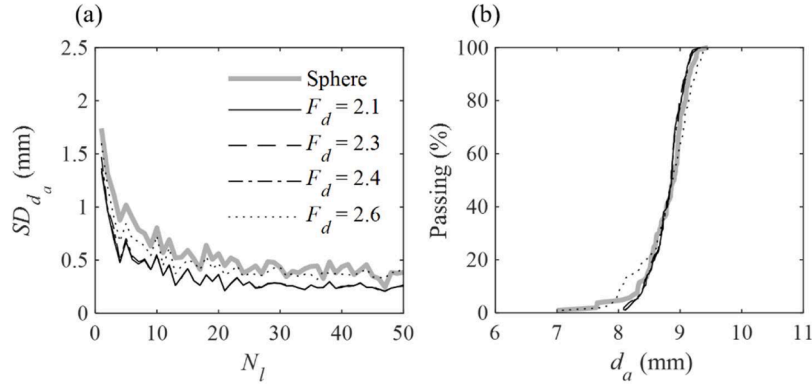
Fig. 2. (a) Influence of the number of Lloyd iterations, N_l, on the standard deviation of aggregate size, SD_{d_a} and (b) aggregate size distribution curves at $N_l = 50$, with the same legend in (a).

illustrative purposes. It is important to ensure that the meshing of aggregates can capture the shape-induced stress concentration effects. The aggregate surface is defined with 642 vertices and discretised into 1280 nearly uniform surficial triangular meshes, directly generated using the published code from the work of Mollon and Zhao [65], which incorporates the concept of geodesic structure. The number of surficial meshes is even more than adequate compared to that used in the work of Wei et al. [75], where around 400 uniformly surficial triangular meshes are defined for the irregular aggregate surface and found sufficient to demonstrate the effects of aggregate shape. Therefore, mesh sensitivity for the aggregate will not be a concern in our case. Then, we import aggregate surfaces, as solid geometries, into the Finite Element Software, ABAQUS/Explicit. On another note, the aggregate shapes are artificially generated based on the statistical information obtained from the actual aggregate shapes [65,76,77]. The actual geometry may differ from the experimental and virtual samples, and our modelling effort focuses on demonstrating the influence of these statistical differences which were observed from experimental datasets. A future study using in situ XCT can supplement our current numerical methods by capturing temporospatial information for detailed validations, which represents a gap to be addressed. The mortar phase is generated by cutting the cubic space with $L = 50$mm using all the solid aggregates. Here, we assume that the mortar phase is homogeneous, without considering the distribution of pores. Based on the surficial mesh size given on the aggregate surface, the tetrahedral element with the size of about 1 mm is used to mesh all solid entities including aggregates and mortar. Representation of ITZ has been debated to the date. The typical value of ITZ thickness varies between $10 \sim 50$ µm [51]. It is challenging to represent the ITZ with physical thickness by the small-scale solid elements [35]. In this study, fracture of ITZ is simulated by the zero-thickness cohesive elements, inserted between the mortar phase and aggregates. Eventually, the meshed mesoscale structure of the concrete specimen is generated as in Fig. 1(d), with about 1420,000 solid elements and about 135,000 cohesive elements for the ITZ. According to Wang et al. [24], 236,260 solid elements are sufficient for the modelling of concrete fracture behaviour, when the mesoscale structure of concrete specimen is of $L = 50$mm and $SF_a = 30\%$. Therefore, no additional effort is dedicated to the mesh sensitivity study. The simulations are conducted in the High-Performance Computing (HPC) platform.

2.2. Constitutive laws for mesoscale model of concrete

Normal-strength concrete is considered here for the modelling of

triaxial tests. The respective constitutive models for mortar, aggregate and ITZ have been decided to appropriately present concrete responses. The concrete damage plasticity (CDP) model has been widely used to simulate concrete damage behaviours [35]. This study focuses only on triaxial tests with low confining pressure, which is significantly lower than the uniaxial strength of normal-strength concrete (approximately 30–40 MPa [78]). Although the entire concrete specimen is subjected to the specified confining pressure, some elements in local regions might experience extremely high pressure, for which we did not optimise the CDP model. For simplicity, as in a previous study [79], the built-in CDP model can be directly considered for our mesoscale structure to capture the general trend of the confined stress–strain response. Greater emphasis is placed on how different aggregate shapes affect the concrete strength under various low confining pressures, rather than on the stress–strain response in a specific region. Here, the built-in CDP model is implemented to the damage behaviour of both mortar phase and aggregates, whereas aggregates are considerably stronger than mortar matrix in normal-strength concrete. The cohesive interface element (CIE) with the traction-separation law is employed to represent ITZ behaviours. Compared with the mortar, ITZ is relatively weaker, partially due to its more porous structures, which is the main reason why crack initiation of concrete generally occurs at ITZ [51]. In the following subsections, the CDP model and cohesive element method are briefly illustrated. More details can be seen in ABAQUS documentation.

2.2.1. CDP model for mortar and aggregate

Compression crushing and tension cracking are considered to be main failure mechanisms given in the CDP model, as in first and third quadrants of Fig. 3(a), respectively. The stress-strain in both quadrants follow the linear elastic relation before ultimate strength in tension, σ_{t0}, and yield stress in compression, σ_{c0}. The compressive response between yield stress, σ_{c0}, and ultimate strength, σ_{cu}, is defined to be strain hardening. For the issue of mesh sensitivity, which is induced by strain localisation [51], it is suggested in some studies to define tensile softening behaviour by specifying stress–displacement curves using the fracture energy criterion instead of stress–strain [51,68,80]. Such considerations are important when using small solid elements in local regions, which are more susceptible to strain localisation and may even lead to unreasonable numerical results [80]. In the current study, our concrete model is meshed with a nearly uniform size, which can be sufficiently used to present the aggregate morphology. Thus, our cases can follow similar works [41,42,81] and directly use stress–strain to define both compressive and tensile softening behaviour in the CDP
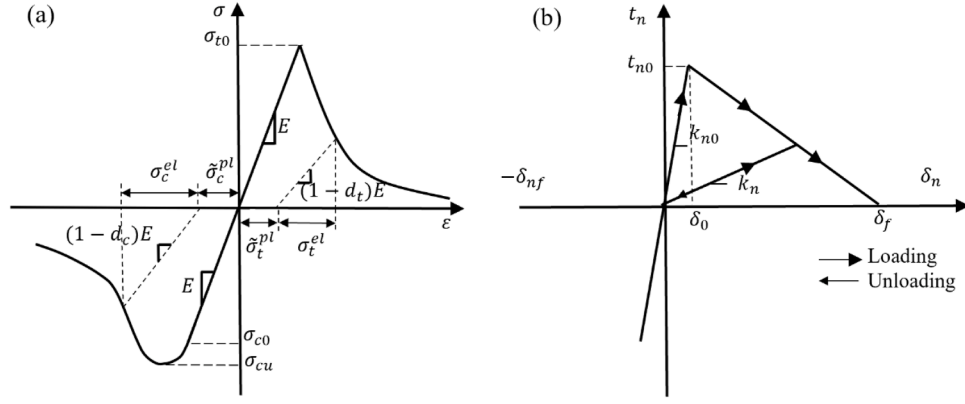
Fig. 3. Schematic diagrams of (a) stress–strain relationship of the CDP model and (b) bilinear traction-separation law of the cohesive element in the normal direction.

model, aiming to obtain an acceptable overall trend in the stress–strain response of concrete, rather than calibrating the model for a specific region. According to Code for Design of Concrete Structures (GB 50010-2010), the compressive strain hardening and softening behaviour are defined as:

below:

$$\sigma_c = (1 - d_c)E(\varepsilon_c - \widetilde{\varepsilon}_c^{pl}), \tag{13}$$

$$\sigma_t = (1 - d_t)E(\varepsilon_t - \widetilde{\varepsilon}_t^{pl}), \tag{14}$$

$$\frac{\sigma_c}{\sigma_{cu}} = \begin{cases} a_a\dfrac{\varepsilon_c}{\varepsilon_{cu}} + (3 - 2a_a)\left(\dfrac{\varepsilon_c}{\varepsilon_{cu}}\right)^2 + (a_a - 2)\left(\dfrac{\varepsilon_c}{\varepsilon_{cu}}\right)^3, \dfrac{\sigma_c}{\sigma_{cu}} \geq 0.4 \text{ and } \dfrac{\varepsilon_c}{\varepsilon_{cu}} \leq 1 \text{ (harderning)} \\[2em] \dfrac{\dfrac{\varepsilon_c}{\varepsilon_{cu}}}{a_d\left(\dfrac{\varepsilon_c}{\varepsilon_{cu}} - 1\right)^2 + \dfrac{\varepsilon_c}{\varepsilon_{cu}}}, \dfrac{\varepsilon_c}{\varepsilon_{cu}} > 1 \text{ (softening)} \end{cases}, \tag{7}$$

where σ_c and ε_c are compressive stress and strain, ε_{cu} is the strain at σ_{cu}, $a_a = 2.4 - 0.0125\sigma_{cu}$ and $a_d = 0.157\sigma_{cu}^{0.785} - 0.905$.

For the tension, beyond the ultimate strength, σ_{t0}, the softening behaviour can be expressed as:

$$\frac{\sigma_t}{\sigma_{t0}} = \frac{\dfrac{\varepsilon_t}{\varepsilon_{t0}}}{\alpha_t\left(\dfrac{\varepsilon_L}{\varepsilon_{t0}} - 1\right)^{1.7} + \dfrac{\varepsilon_t}{\varepsilon_{t0}}}, \tag{8}$$

where σ_t and ε_t are tensile stress and strain, ε_{t0} is the strain at σ_{t0}, and $\alpha_t = 0.312\sigma_{t0}^2$.

The stress-strain as defined above can be also converted into the stress-plastic strain curve, by following equations:

$$\widetilde{\varepsilon}_c^{pl} = \widetilde{\varepsilon}_c^{in} + \varepsilon_{0c}^{el} - \varepsilon_c^{el}, \tag{9}$$

$$\widetilde{\varepsilon}_t^{pl} = \widetilde{\varepsilon}_t^{ck} + \varepsilon_{0t}^{el} - \varepsilon_t^{el}, \tag{10}$$

where $\widetilde{\varepsilon}_c^{pl}$ and $\widetilde{\varepsilon}_t^{pl}$ are equivalent plastic strain tensor in compression and tension, $\widetilde{\varepsilon}_c^{in}$ and $\widetilde{\varepsilon}_t^{ck}$ are inelastic strain in compression and cracking strain in tension, and ε_{0c}^{el}, ε_c^{el}, ε_{0t}^{el} and ε_t^{el} are defined as below:

$$\varepsilon_{0c}^{el} = \frac{\sigma_c}{E}, \ \varepsilon_c^{el} = \frac{\sigma_c}{(1 - d_c)E}, \tag{11}$$

$$\varepsilon_{0t}^{el} = \frac{\sigma_t}{E}, \ \varepsilon_t^{el} = \frac{\sigma_t}{(1 - d_t)E}, \tag{12}$$

where d_c and d_t are damage variables for compression and tension, respectively, and E is Young's modulus. Eventually, the stress-strain relation under tension and compression loading can be obtained as

where $\varepsilon_c = \varepsilon_{0c}^{el} + \widetilde{\varepsilon}_c^{in}$ and $\sigma_t = \varepsilon_{0t}^{el} + \widetilde{\varepsilon}_t^{ck}$.

For material properties of mortar and aggregate, most inputs for the CDP are given with acceptable values from previous literature [35,51, 82], as listed in Table 1. Additionally, other five parameters for the CDP model, the dilation angle, plastic potential eccentricity, ratio of compressive strengths under biaxial and uniaxial loading, ratio of the second stress invariant on the tensile meridian to that on the compressive meridian, and viscosity parameter, have the corresponding values of 35°, 0.1, 1.16, 0.667 and 0.0005 [35,51], and are used for both concrete phases here.

2.2.2. Cohesive interface element method for ITZ

For the cohesive element, the traction-separation law illustrates that one normal and two shear tractions acting on adjacent surfaces result in

Table 1
Material properties of concrete constituents.

Component	Material property	Value
Mortar/Aggregate (Concrete damage plasticity, CDP)	Density, ρ (kg/m^3)	2200/ 2600
	Young's modulus, E (GPa)	30/70
	Poisson's ratio, v	0.2/0.2
	Ultimate strength in compression, σ_{cu} (MPa)	45/80
	Ultimate strength in tension, σ_{t0} (MPa)	4/10
ITZ (Cohesive interface element, CIE)	Initial stiffness, k_{n0}, k_{s0}, k_{t0}(N/m^3)	1×10^{13}
	Normal strength, t_{n0}, (MPa)	2.4
	Shear strength, t_{s0},t_{t0} (MPa)	7.2
	Fracture energy, $G_{f,n}$, $G_{f,s}$, $G_{f,t}$ (N/m)	30
Fracture (Broken CIE)	Friction coefficient	0.3

separations, such as crack initiation and evolution [83]. For simplicity, we consider the bilinear traction-separation law to describe the response of cohesive elements, as in Fig. 3(b). The linear elastic behaviour after the damage initiation is followed by linear softening. It is noted for Fig. 3 (b) that here only shows the normal direction with the notation $*_n$. The first quadrant of Fig. 3(b), if $*_n$ is replaced by $*_s$ and $*_t$ as shown in context, can be also used as first and third quadrants of schematic diagram to illustrate the traction-separation in two shear directions, and the corresponding diagrams in both directions are not provided here. In this study, the criterion for damage initiation is the quadratic nominal stress law, as given by:

$$\left\{\frac{\langle t_n \rangle}{t_{n0}}\right\}^2 + \left\{\frac{t_s}{t_{s0}}\right\}^2 + \left\{\frac{t_t}{t_{t0}}\right\}^2 = 1, \tag{15}$$

where t_n is normal traction, t_s and t_t are two shear tractions, t_{n0}, t_{s0} and t_{t0} are corresponding cohesive strengths and critical values for damage initiation, and $\langle \cdot \rangle$ is the Macaulay bracket defined as:

$$\langle t_n \rangle = \begin{cases} t_n, & t_n \geq 0 \text{ (tension)} \\ 0, & t_n < 0 \text{ (compression)} \end{cases}. \tag{16}$$

Fracture energy, G_f, is the area under the curve representing separation, δ, and traction, $t(\delta)$, and it can be determined using the cohesive strength, t_0, and failure separation, δ_f, in either normal or shear directions, as below:

$$G_f = \int_0^{\delta_f} t(\delta)d\delta = \frac{1}{2}t_0\delta_f. \tag{17}$$

The damage variable, d_{CIE}, as function of effective relative displacement, δ_m, is introduced to describe the linear softening branch representing the damage evolution, and defined as:

$$d_{\text{CIE}} = \frac{\delta_{mf}(\delta_m - \delta_{m0})}{\delta_m(\delta_{mf} - \delta_{m0})}, \tag{18}$$

$$\delta_m = \sqrt{\langle \delta_n \rangle^2 + \delta_s{}^2 + \delta_t{}^2}, \tag{19}$$

$$\langle \delta_n \rangle = \begin{cases} \delta_n, & \delta_n \geq 0 \text{ (tension)} \\ 0, & \delta_n < 0 \text{ (compression)} \end{cases}, \tag{20}$$

where δ_n, δ_s and δ_t are separation in one normal and two shear directions, δ_{m0} and δ_{mf} are effective relative displacement at damage initiation and final failure. During the damage evolution, the stiffness degradation is controlled by d_{CIE}, and the current stiffness in one normal and two shear directions k_n, k_s, k_t are given by:

$$k_n = (1 - d_{\text{CIE}})k_{n0}, k_s = (1 - d_{\text{CIE}})k_{s0}, k_t = (1 - d_{\text{CIE}})k_{t0}, \tag{21}$$

where k_{n0}, k_{s0} and k_{t0} are initial cohesive stiffness correspondingly, and $k_{n0} = k_{s0} = k_{t0}$ is assumed in this study. Damage-affected tractions, t_n, t_s and t_t, are defined as:

$$t_n = \begin{cases} (1 - d_{\text{CIE}})\overline{t_n}, & \overline{t_n} \geq 0 \\ \overline{t_n}, & \overline{t_n} < 0 \end{cases},$$
$$t_s = (1 - d_{\text{CIE}})\overline{t_s}, \tag{22}$$
$$t_t = (1 - d_{\text{CIE}})\overline{t_t},$$

where $\overline{t_n}$, $\overline{t_s}$ and $\overline{t_t}$ are traction components calculated based on the elastic-displacement behaviour for the current separations without damage.

For the ITZ, input values for material parameters of the cohesive element are listed in Table 1, as in some studies [35,51,82]. The energy-based crack evolution is considered for the linear softening region. The Benzeggagh-Kenane criterion [84] is used for the mixed mode

behaviour, and for simplicity, fracture energy G_f are assumed to be the same in normal $G_{f,n}$ and two shear directions $G_{f,s}$ and $G_{f,t}$, $G_f = G_{f,n} = G_{f,s} = G_{f,t}$.

2.3. Triaxial loading conditions

As shown in Fig. 1(d), the concrete model is loaded under triaxial compressive stresses of σ_1, σ_2 and σ_3, where σ_1, σ_2 and σ_3 are referred to principal stresses. In this study, $\sigma_1 > \sigma_2 = \sigma_3 = \sigma_L \geq 0$MPa and only confining pressure, σ_L, less than uniaxial compressive strength of concrete are considered. Though the explicit scheme is used here for its efficiency of handling multiple contacts, the modelling focuses on the quasi-static triaxial test. As the ABAQUS/Explicit is a dynamic solver, the loading rate on the concrete model needs to be carefully selected to avoid considerable initial effects; we have ensured that the ratio of the total kinetic energy to internal energy is always below 5 % in all simulations.

The loading is implemented in two steps, which are carried out sequentially in the simulation without any coupling settings. As shown in Fig. 1(d), all nodes at the bottom are fixed in the direction of σ_1 (i.e., the y-direction). In the first step, the confining pressure, σ_L, is applied to the top and side faces of the cubic concrete specimen, linearly increasing to the given value within 0.001 s. In the second step, the stress σ_1 for the top surface is increased to $\sigma_1 + \sigma_q$, where σ_q is the deviatoric stress applied using a velocity-controlled method. Meanwhile, confining pressure σ_L keeps acting to other confined faces (i.e., $\sigma_2 = \sigma_3 = \sigma_L$), as propagated from the end of first step. The velocity of the nodes on the top surface is linearly ramped up to 25 mm/s within 0.001 s and then held constant until the end of the second step. In this study, the given confining pressures $\sigma_L = 0, 5, 10, 15, 20, 25$MPa are considered, unless otherwise emphasised. To obtain the stress-strain data under different σ_L, the entire time of the second step is set to 0.02 s. It is noted that the uniaxial compression tests correspond to cases with $\sigma_L = 0$MPa.

3. Results and discussion

In this section, using our established model, numerical analyses are performed to investigate the macro- and micro-mechanical responses of concrete under various confining pressures and aggregate shapes. The macroscopic responses of concrete under uniaxial and triaxial stress conditions are presented in Section 3.1. Particular focus is placed on the relation between the macro-strength of concrete and confining pressure, which will be compared with existing experimental data. To explore the underlying micro-mechanisms behind the influence of aggregate shape on these relations, quantitative evidence is examined through local stress distribution, local damage and crack clusters in Sections 3.2 to 3.4, respectively.

3.1. Stress–strain responses

Based on the above-established modelling, firstly we can obtain the σ_L-influenced axial stress (σ_1) – strain (ε_1) curves for the concrete with various shaped inclusions, as the specimens with sphere, $F_d = 2.1$, $F_d = 2.3$, $F_d = 2.4$, and $F_d = 2.6$ shown in Fig. 4(a). Therein, σ_1 is defined as F/A, with F being the sum of nodal reaction force on the top boundary where the velocity boundary condition is inserted, and $A = 50 \times 50$mm^2 is the initial cross-section area, and ε_1 is calculated as the ratio of nodal displacement to the initial side length of the specimen. For the obtained stress–strain curves, our results for uniaxial tests show good agreement with the experimental work of Lowes et al. [85]. For the triaxial tests, it is challenging to find experimental results that exactly match the same combination of aggregate solid fraction, aggregate size, specimen dimensions, and confining pressures used in our model. We acknowledge this as a limitation in validating our model from the stress–strain perspective. Thus, Fig. 4(a) is primarily used to demonstrate that our model can capture the general characteristics of the triaxial response of
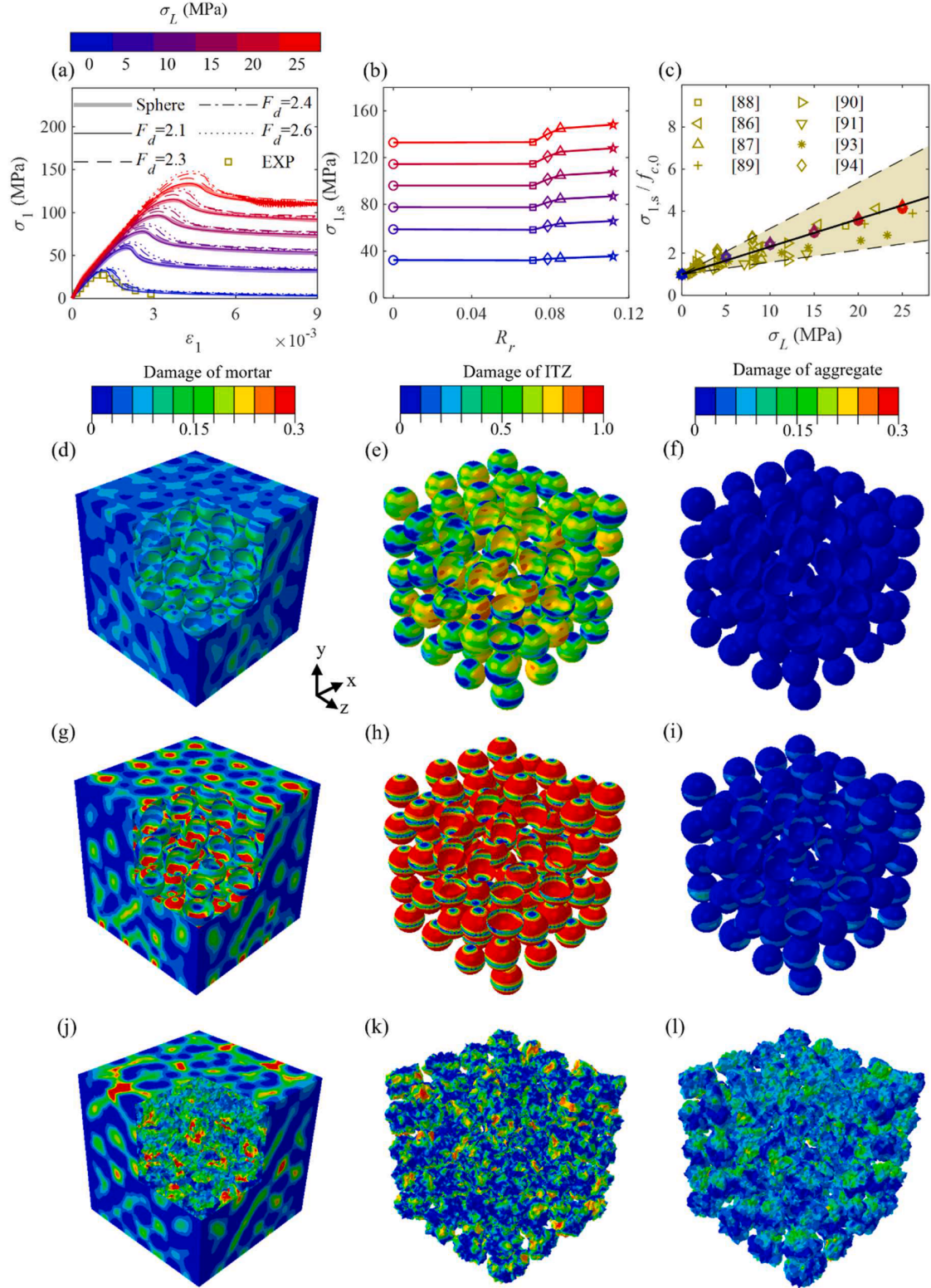
Fig. 4. (a) Typical axial stress–strain curves for different aggregate shapes and confining pressures, where EXP shows results from the experiments of Lowes et al. [85], (b) compressive strength, $\sigma_{1,s}$, versus relative roughness, R_r, where the markers from left to right represent cases of sphere, $F_d = 2.1$, $F_d = 2.3$, $F_d = 2.4$ and $F_d = 2.6$, respectively, (c) relations between normalised strength, $\sigma_{1,s}/f_{c,0}$, and confining pressure, σ_L, where the black line fits FEM simulations, and dashed black lines are for fitted upper and lower bounds of experimental data, and (d-l) damage field distributions of mortar, ITZ and aggregate at the compressive strength, where (d-f) are for the uniaxial test, (g-l) are for the triaxial test with $\sigma_L = 25$MPa; (d-i) are for the sphere and (j-l) are for aggregates with $F_d = 2.6$.

concrete. As an alternative approach for model validation, the relation between concrete strength and confining pressure, as our main basis of investigation into the influence of aggregate shape, will be compared with existing data in the following.

As shown in Fig. 4(a), with a rising confining pressure, the peak value of σ_1 (i.e., compressive strength, $\sigma_{1,s}$) are increased, and the post-peak softening turns to be flatter. Such an increase of $\sigma_{1,s}$ in the triaxial test can be explained by severer damage in all three phases as shown in Fig. 4 (g–i), when compared to the uniaxial test in Fig. 4(d–f). In Fig. 4(a), another noticeable point is that rougher aggregate shapes with higher F_d result in higher $\sigma_{1,s}$. That is because higher F_d induces higher stress concentrations near aggregate surfaces, which may lead to more fractures propagating across the strongest phase, aggregate, rather than along the weakest phase—ITZ, as demonstrated in Fig. 4(g–l); as a result, the macroscopic strength of concrete is enhanced. This influence could be further enhanced by higher confining pressure, σ_L, as illustrated in Fig. 4(b). Wei et al. [22] also found more roughness-induced higher uniaxial compressive strength, $f_{c,0}$, in numerical uniaxial tests on mesoscale concrete samples. This pronounced effect due to increased confining pressure may be rooted in more stress concentrations under triaxial states.

The combined effects of confining pressures and aggregate morphology features, $f_{c,0}$-normalised $\sigma_{1,s}$ versus σ_L are provided in Fig. 4 (c). Our numerical results are also plotted against some existing experimental works focusing on various strength-dependent factors including normal [86–89] or high-strength concrete [90,91], confinement [92], supplementary materials [93], and dynamic loading impacts [94]. Besides the consistence with the experimental results, it is surprising that all data pertinent to various inclusion shapes and confining pressures collapses well onto a single line with $R^2 \approx 1$, as below:

$$\sigma_{1,s}\big/f_{c,0} = k\cdot(\sigma_L / \sigma_0) + 1, \tag{23}$$

where σ_0 is 1 MPa for normalisation, and $k = 0.13$ is the fitting parameter. Failure criterions have been analytically or empirically proposed to predict $\sigma_{1,s}$ by σ_L, such as unmodified [95] and modified Mohr-Coulomb [96], Newman [97], Leon-Pramono [98] criterions and others [99]. Compared with all these criterions, our model only contains one fitting parameter. The following sections are dedicated to untangling why and how the macroscopic scaling law bridging $\sigma_{1,s}$ and σ_L holds for concrete with distinctive inclusions, with the micro perspectives of local stress, damage evolutions and crack patterns.

3.2. Local stress distributions

The stress distribution and its evolution during triaxial loading are focused on the mortar phase. As a continuous medium connecting discretely distributed aggregates surrounded by the ITZ, the mortar has the stress distribution that results from aggregate-to-aggregate and aggregate-to-mortar interactions, in addition to external loading, thus reflecting the influence of aggregate shape. The stress distribution in the host matrix has been successfully used to explain the 2D macro failure of materials with a disordered spatial distribution of circular flaws [63]. Such an approach using the stress distribution will be extended to more general cases of concrete, where the mortar is taken as host matrix containing the aggregate and surrounding ITZ, to gain the insight into the fracture process of concrete with different aggregate shapes. Here, the evolution of stress distribution in the mortar is focused during the loading with an increasing ratio of macroscopic stress to compressive strength, $\sigma_1/\sigma_{1,s} \in [0.1, 1]$, where the confining stage (i.e., $\sigma_1 \leq \sigma_L$) is excluded. Given the mean stress of element in the mortar phase, σ_{pe}, obtained from the simulation results, probability density function (PDF) is plotted for its normalised value, $\sigma_{npe} = (\sigma_{pe} + 2\sigma_{t,0})/f_{c,0}$, where $\sigma_{t,0}$ is tensile strength as given in Table 1, and the shift of $2\sigma_{t,0}$ is used to remove the negative value and allows the PDF of σ_{npe} plotted in log-log scale, $f_{c,0}$ (i.e., $\sigma_{1,s}$ at $\sigma_L = 0$ MPa) is uniaxial strength of concrete with

the influence of aggregate shapes in terms of relative roughness, R_r, as shown in Fig. 4(b), and normalising $f_{c,0}$ scales element stress to minimise the quantitative differences between aggregate shape, making it more effective for focusing on how the aggregate shape affects the heterogeneity of stress distribution during the triaxial loading. The PDF at each $\sigma_1/\sigma_{1,s}$ is calculated based on the element volumes, showing its dependences on the aggregate shape and confining pressure by log-log plots, as shown in a few examples in Fig. 5(a–c). To characterise the PDF, the following statistical indices are introduced for Fig. 5(d–f) as:

$$\text{Kurtosis}: K_{\text{npe}} = \frac{\frac{1}{n}\sum_{i=1}^{n}\left(\sigma_{\text{npe}} - M_{\text{npe}}\right)^4}{\left(\frac{1}{n}\sum_{i=1}^{n}\left(\sigma_{\text{npe}} - M_{\text{npe}}\right)^2\right)^2} - 3 \tag{24}$$

$$\text{Skewness}: S_{\text{npe}} = \frac{\frac{1}{n}\sum_{i=1}^{n}\left(\sigma_{\text{npe}} - M_{\text{npe}}\right)^3}{\left(\sqrt{\frac{1}{n}\sum_{i=1}^{n}\left(\sigma_{\text{npe}} - M_{\text{npe}}\right)^2}\right)^3} \tag{25}$$

and

$$\text{Standard deviation}: SD_{\text{npe}} = \sqrt{\frac{1}{n-1}\sum_{i=1}^{n}\left(\sigma_{\text{npe}} - M_{\text{npe}}\right)^2}, \tag{26}$$

where the M_{npe} is the mean value of element-level stress σ_{npe}.

At almost linear elastic regime ($\sigma_1/\sigma_{1,s}= 0.2$), PDF in Fig. 5(a) shows that most element stresses σ_{npe} are concentrated within a small range. The kurtosis, K_{npe}, and skewness, S_{npe}, which is used to indicate the heterogeneity of stress distribution in mortar, exhibit significant variation across different aggregate shapes, as shown in the Fig. 5(d) and (e), respectively. That is due to the presence of extreme values of σ_{npe} in the right tails of PDF, showing a dependency on the aggregate shape. The rougher aggregates induce the higher concentrated stresses on mortar elements adjacent to their boundaries and can result in greater heterogeneity of stress distribution in mortar, as also evidenced by higher value of K_{npe} and S_{npe}. In triaxial tests with increasing confining pressure, although the stress near aggregate boundaries intensifies and shifts the PDF to the right, the overall trend of PDF in Fig. 5(a) remains nearly unchanged for all aggregate shapes, showing decreasing dependency on the shapes. This is also reflected in insignificant variation of K_{npe} and S_{npe} at $\sigma_1/\sigma_{1,s}= 0.2$ across different confining pressures, suggesting the similar influence of aggregate shape on heterogeneity of stress distribution in mortar.

Beyond the elastic region, as $\sigma_1/\sigma_{1,s}$ increases, the overall stress in the mortar improves to varying degrees, leading to a broader range of the PDF of σ_{npe}, as seen in the comparison between Fig. 5(b) or (c) and (a). Simultaneously, the standard deviation, SD_{npe}, shows a continuous increase, accompanied by a progressively more pronounced effect of confining pressure. This is because the stress in the mortar tend to increase and propagate in a restricted direction due to the confining pressure, leading to a more heterogeneous stress distribution. The difference in the PDF between aggregate shapes may be reduced, as indicated by K_{npe} and S_{npe}, which converge to their respective values. This suggests that although the initial influence of aggregate shape on the heterogeneity of stress distribution gradually weakens, the relative differences can still be observed under different confining pressures. As seen in Fig. 5(g–l), with increasing $\sigma_1/\sigma_{1,s}$, the enhanced stress gradually propagates to other regions of the mortar, causing the heterogeneity of the stress distribution to extend over a wider high-stress area, where the shape-induced stress concentration effects on mortar elements become less pronounced compared to those at the initial loading stage.

When $\sigma_1/\sigma_{1,s}$ approaches 1 (or approaching the respective uniaxial compressive strength), the confining pressure becomes a more dominant factor influencing the heterogeneity of stress distribution, showing a universality across different aggregate shapes, as more apparently
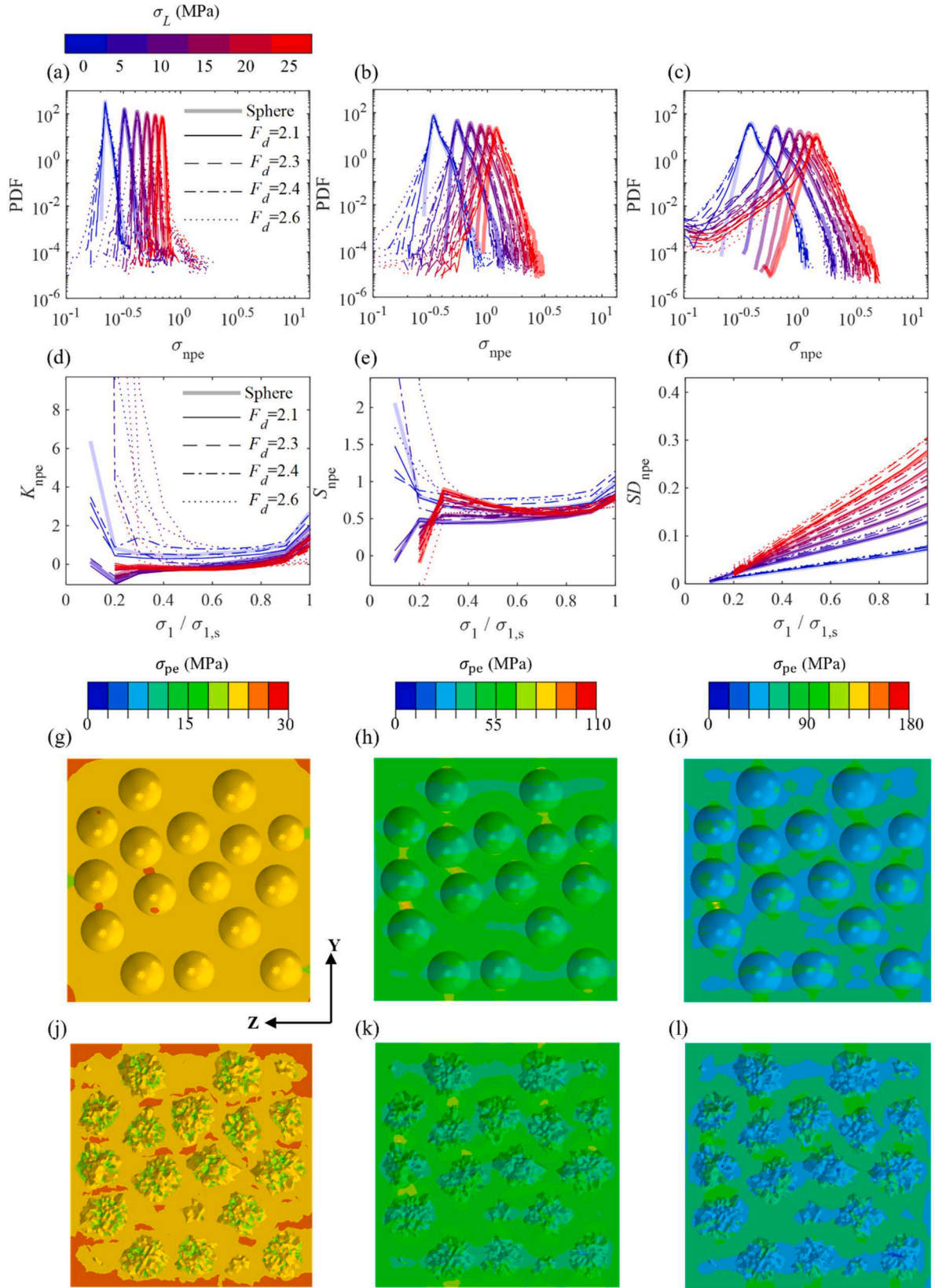
Fig. 5. Probability density functions (PDFs) of normalised mean stress, σ_{npe}, of mortar elements at (a) $\sigma_1/\sigma_{1,s} = 0.2$, (b) $\sigma_1/\sigma_{1,s} = 0.8$ and (c) $\sigma_1/\sigma_{1,s} = 1$, all using the legends from (a), and variations of (d) kurtosis, K_{npe}, (e) skewness, S_{npe}, and (f) standard deviation, SD_{npe}, of σ_{npe} with $\sigma_1/\sigma_{1,s}$, all using the legends from (d), and (g-l) distribution of mean stress, σ_{pe}, in mortar on the y-z plane (i.e. midplane of the concrete specimen) at $\sigma_L = 25$ MPa: (g) and (j) are for $\sigma_1/\sigma_{1,s} = 0.2$, (h) and (k) are for $\sigma_1/\sigma_{1,s} = 0.8$, (i) and (l) are for $\sigma_1/\sigma_{1,s} = 1$, (g-i) and (j-l) are for cases of sphere and $F_d = 2.6$, respectively.

evidenced by SD_{npe} in Fig. 5(e).

Finally, at $\sigma_1/\sigma_{1,s}=1$, the heterogeneity of stress distribution in mortar is similar across different aggregate shapes, and this aligns with the universal scaling law expressed by Eq. (23) and in Fig. 4(c). However, this similarity in stress heterogeneity does not explain the reason

that rougher aggregates lead to a greater overall concrete strength, as illustrated in Fig. 4(b). When concrete approaches its failure strength, it transitions from linear to non-linear regions with possible damage initiation or propagation within the material phases. The influence of material properties and / or morphology have been used to analyse
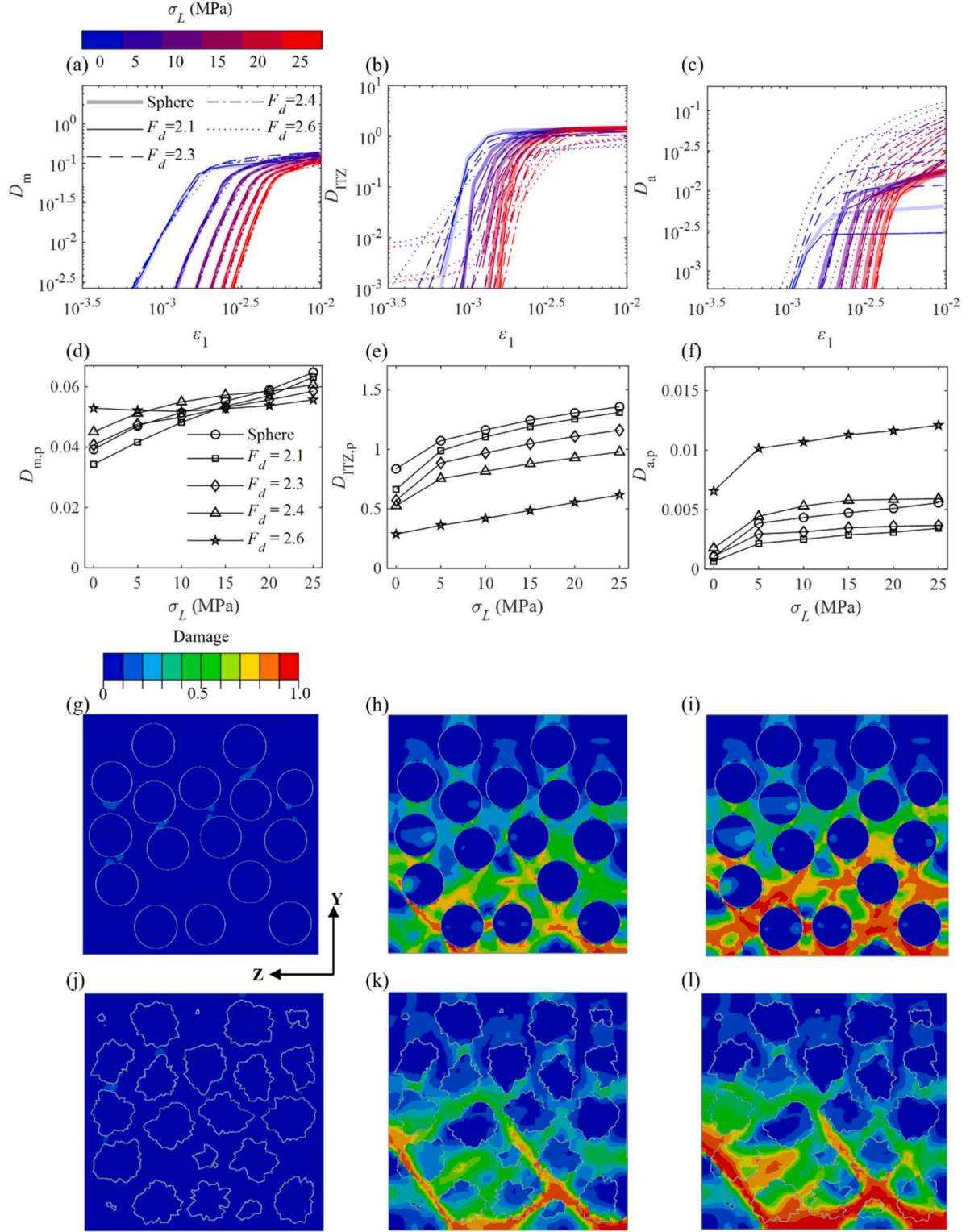

Fig. 6. (a-c) Evolutions of damage in mortar, ITZ and aggregate with the axial strain, ε_1, all using the legend from (a), and (d–f) variation in damage in mortar, ITZ and aggregate corresponding to the compressive strength with σ_L, all using the legends from (d), and damage field distribution on y-z plane (i.e. midplane of the concrete specimen) at $\sigma_L = 25$ MPa: (g) and (j) are for $\varepsilon_1 = 0.003$, (h) and (k) are for $\varepsilon_1 = 0.006$, (i) and (l) are for $\varepsilon_1 = 0.009$, (g-i) and (j-l) are for cases of sphere and $F_d = 2.6$.

damage mechanisms to interpret how the evolution of internal structure affects the macroscopic behaviour of concrete [22,35]. It is worth noting here that our focus on the stress distribution in the mortar alone is intended to determine whether this approach, similar to that of Laubie et al. [63], is applicable to our analysis. The investigation of the heterogeneity of stress distribution will not be extended to other material phases of concrete. We found that while this approach effectively explains the universal scaling law, it fails to account for the influence of aggregate shape on the macroscopic strength of concrete. Therefore, it is necessary to investigate the underlying reasons for both issues from an alternative perspective, focusing on the assessment of local damage, as discussed in the following section.

3.3. Damage evolutions

The local damage of concrete is investigated to understand how different material phases contribute to the damage, providing a more accurate representation of the macroscopic behaviour to illustrate its universality. Here, the damage in different material phases, mortar, ITZ, and aggregate are expressed as D_m, D_{ITZ}, and D_a, respectively, and can be quantified as below:

$$\frac{\sum_{i=1}^{N} d_i V_i}{V_c} \text{ or } \frac{\sum_{i=1}^{N} d_i S_i}{S_c}, \tag{27}$$

where d_i is the element-level damage of i th element, V_i is the volume of i th solid element for mortar or aggregate, S_i is the area of i th cohesive interface element (CIE) representing the ITZ, and V_c and S_c are the volume and surface area of cubic specimen of concrete, respectively.

To investigate whether damages have any universality during triaxial loading, the evolution of D_m, D_{ITZ} and D_a are computed using values at 30 uniform increments within the range of axial strain, $\varepsilon_1 \in [0.0005, 0.01]$. Fig. 6(a–c) in log-log scale highlight effects of confining pressure and aggregate shape. When damages increase with the strain, D_{ITZ} evolves fastest and reaches the maximum first due to the weakest intrinsic fracture strength, followed by D_m and D_a. This also explains why damage originates from areas adjacent to aggregate boundaries and then spreads to other regions of the material phases, as shown in Fig. 6 (g-l). With an increased σ_L, a significant delay in the damage evolution can be observed. That is because the enhanced material strength due to σ_L makes it less prone to inelastic deformation, and the failure mode of the material becomes more ductile, typically requiring greater deformation of elements for the onset of damage. Among all material phases, only the damage evolution of mortar remains quite similar across aggregate shape, exhibiting a universal behaviour governed by the confining pressure σ_L. However, this universality is absent in the damage evolution of the ITZ and aggregates due to significant variations in aggregate shapes, as shown in Fig. 6(b-c). In particular, under larger strain, greater damage propagation from the ITZ into the aggregates is observed in cases with rougher aggregate shapes, as seen in Fig. 6(g–l). These observations contradict the universality of the scaling law expressed in Eq. (21). To address this, the following focus will be on investigating how material phases respond at a specific point, i.e., the concrete strength, instead of the entire loading process.

To find underlying reasons behind the scaling law, damages in mortar, $D_{m,p}$, ITZ, $D_{ITZ,p}$, and aggregate, $D_{a,p}$, at the respective ultimate compressive strength are provided in Fig. 6(d–f). When an increase of confining pressure, σ_L, enhances the concrete strength, it also results in greater damage within each material phases. It is because at higher σ_L, reaching the compressive strength requires more deformation, as shown in Fig. 4(a), during which the intensified overall stress within the material phases promotes the initiation or propagation of damage within elements. With an increasing value, the $D_{m,p}$ shows insignificant dependency on the aggregate shape, due to the similar heterogeneity of stress distribution in the mortar at the compressive strength (i.e., $\sigma_1/\sigma_{1,s}=1$) in Fig. 5, indicating comparable levels of damage. More noticeable

effects of aggregate shape can be observed in $D_{ITZ,p}$ and $D_{a,p}$, which shows the competitive relation with an increasing F_d of aggregate. This aligns with the findings of Wei et al. [22], which focused only on uniaxial compressive tests. However, this study also find that this competition extends to triaxial tests and remains universal across various confining pressures.

For rougher aggregates, higher stress concentration can be induced. The presence of confining pressure further amplifies this effect by preventing the material from expanding laterally and increasing localised stresses. This further promotes the fracture propagation from the ITZ to the aggregates. As a result, with an increasing F_d of the aggregate, $D_{ITZ,p}$ decreases while $D_{a,p}$ increases. The tendencies become more pronounced as overall damage increases with increasing σ_L. The relative damage change in different phases explains why rougher aggregates cause the more significantly enhanced concrete strength at higher σ_L, as shown in Fig. 4(b). Due to its fully convex shape, damage in spherical aggregate, which is even greater than in some realistic aggregates, causes $D_{ITZ,p}$ and $D_{a,p}$ to deviate from the competitive relation for realistic shapes. The greater surface roughness of realistic aggregate with higher F_d causes fracture propagation to concentrate in more localised areas (e.g., sharp corners or edges), resulting in an almost proportional increase in $D_{a,p}$. The universality of the competitive relation between damage levels in ITZ and aggregates across σ_L indicates that the effect of aggregate roughness on concrete strength can be mapped from triaxial to uniaxial tests. Thus, when the $\sigma_{1,s}/f_{c,0}$ is used in Eq. (23), it can reduce the dependence of relation between σ_L and $\sigma_{1,s}$ on the aggregate shape, allowing Eq. (23) to be applied to predict the σ_L-dominated concrete strength for different aggregate shapes, whilst the shape effects being fully captured by the uniaxial compressive strength.

3.4. Crack patterns

At the final loading stage, we assess the crack pattern of concrete subjected to triaxial loading. Most existing mesoscale studies rely only on visual observation to compare and discuss crack patterns [24,35]. We attempt to improve such an investigation by introducing quantitative analyses of the crack clusters in each material phase. Here, the macro-crack is assumed to form at the axial strain, $\varepsilon_1 = 0.009$. In the modelling, there is no precisely defined damage threshold for identifying cracked elements. However, some existing numerical studies have used the damage value of elements to characterise cracking patterns in concrete, commonly adopting a threshold of 0.9 [35,41,42,73]. Following this convention, solid elements or CIEs with damage values exceeding this threshold, considered as cracked elements, are isolated from each material phase of concrete. The contact between crack clusters in mortar and aggregate is determined by the face-to-face contact of solid elements, while in the ITZ, it is determined by the edge-to-edge contact of zero-thickness CIEs. Our in-house algorithm for both contact detection methods, which are implemented in MATLAB, follows the main workflow outlined below:

(1) All cracked elements of each material phase are collected into a set, $T_E = \{E_i | i = 1, 2, ..n\}$, where i is the element index. Each solid element or CIE can be represented using a 4×3 or 3×2 matrix, where each row contains node indices representing the face or edge of the element.
(2) We check whether any single element in T_E is in contact with other elements. The contact criterion is defined as follows: any two solid elements (or CIEs) that share the same row of node indices are considered to be in face-to-face (or edge-to-edge) contact.
(3) The connection elements are identified as clusters for different material phases.

Once the above processes are completed, each cluster size of mortar, $V_{f,m}$, ITZ, $S_{f,ITZ}$, or aggregate, $V_{f,a}$ is determined by summing the volume
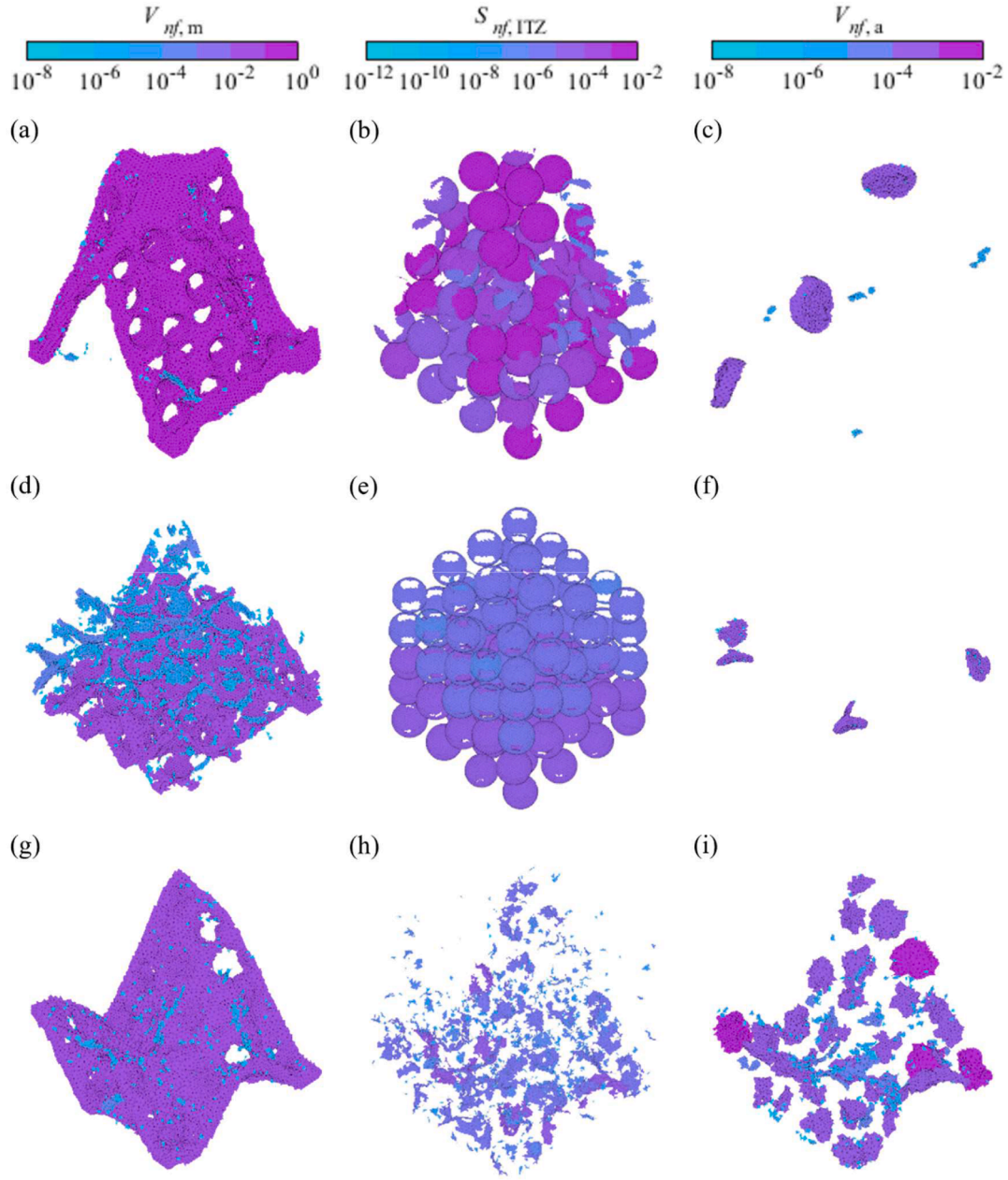
Fig. 7. Crack patterns of mortar, ITZ and aggregate, where (a-c) are for the uniaxial test, (d-i) are for the triaxial tests with $\sigma_L = 25$MPa, (a-f) are for the sphere and (g-i) are for aggregates with $F_d = 2.6$, and three colours bars from left to right sequentially represent the relative size (i.e., area/volume) of crack cluster of mortar, $V_{nf,m}$, ITZ, $S_{nf,ITZ}$ and aggregate, $V_{nf,a}$.

or area of elements within the same cluster. The normalisation is conducted as $V_{nf,m} = V_{f,m}/V_c$, $S_{nf,ITZ} = S_{f,ITZ}/S_c$, and $V_{nf,a} = V_{f,a}/V_c$, shown in Figs. 7 and 8.

For cases with spherical aggregates, cracks in the uniaxial test freely develop along inclined planes, forming distinct V-shaped branches that cross diagonally, particularly prominent in the mortar, as shown in Fig. 7(a). As observed in the comparison between Fig. 7(d-f) and Fig. 7 (a-c), differences in crack morphology between uniaxial and triaxial tests are primarily found in the mortar and ITZ, while negligible in the aggregate due to the minimal crack volume. With $\sigma_L = 25$ MPa, along the increased crack area in the ITZ, cracks in the mortar become less inclined and exhibit a more diffuse pattern, as shown in Fig. 7(d), due to the constraint on lateral deformation imposed by the confining pressure.

For the cases with realistic aggregate under triaxial loading, damage during the post-peak stage continues to intensify in the already affected local regions at or around the sharp corners or edges of aggregates, and propagates along these regions deeper into the aggregate, leading to the new cracks or the expansion of existing cracks into larger areas within aggregates. When $\varepsilon_1 = 0.009$, as shown in Fig. 7(d-f), cracks in the ITZ are distributed in spatially dispersed clusters, while a considerable volume of cracks is observed within the aggregates. In contrast, as shown in Fig. 7(e-f) for cases with spherical aggregates, due to lower stress concentration, damage tends to be more uniform on the spherical surface, leading to spatially continuous and extensive cracks in the weakest phase—ITZ. In the strongest phase—aggregate, only a few local regions reach the critical damage threshold (i.e., 0.9) and form cracks.

PDF is plotted for the relative crack cluster size, which is evenly divided in logarithmic space. It is calculated based on the cluster counts within each bin width and provided in Fig. 8(a–c). The PDFs reveal that smaller relative crack cluster sizes occur more frequently in material
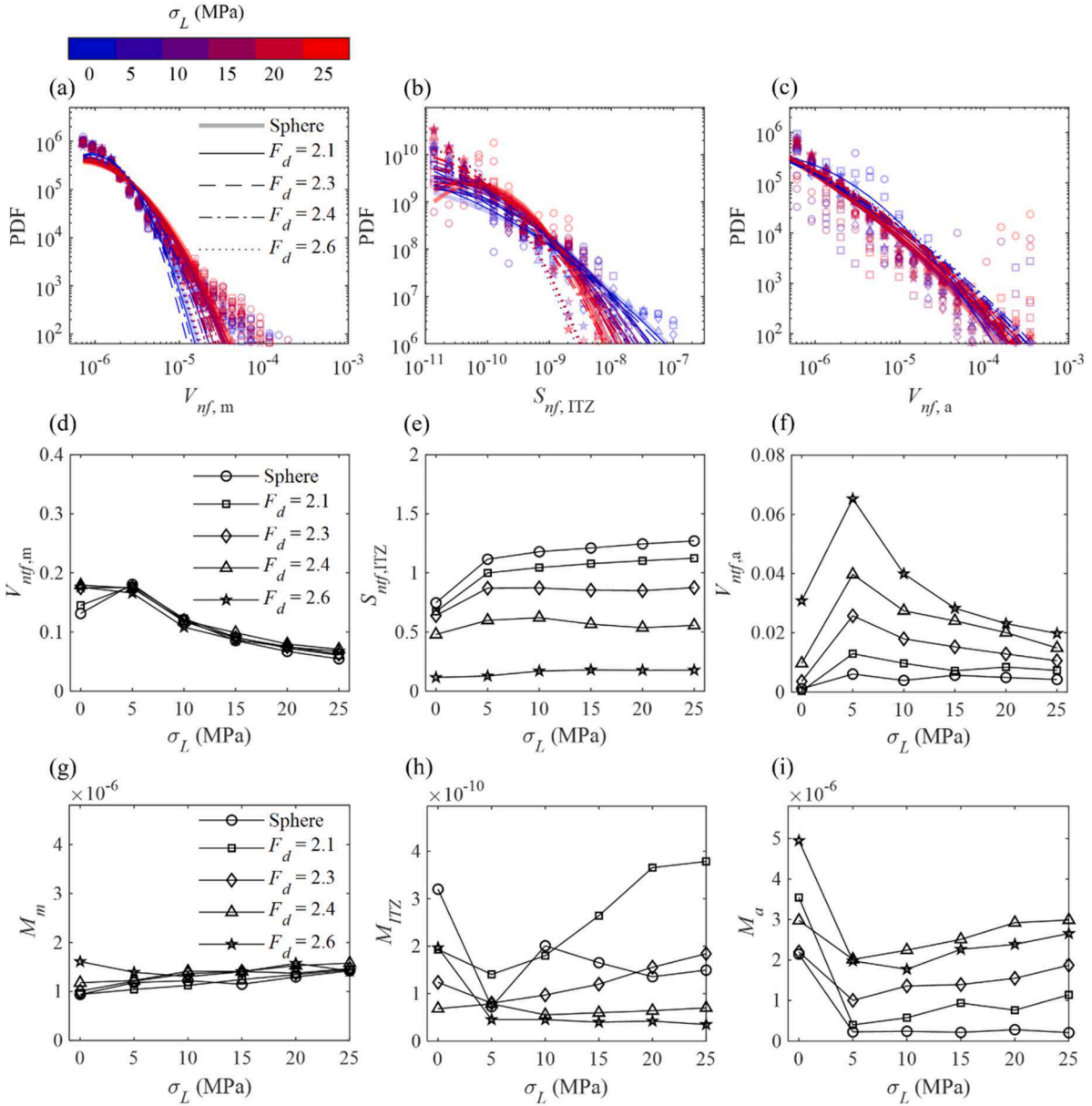
Fig. 8. (a–c) Probability distributions of relative size of crack clusters of mortar, ITZ and aggregate, maker shapes for data point follow the legend in (d), legends in (a) for lognormal fittings is also used for (b-c), (d-f) variations in relative total crack volume/area of mortar, ITZ and aggregate with respect to σ_L, all using the legends from (d), and (g-i) variations in mean value of lognormal fittings to PDF for mortar, ITZ and aggregate with respect to σ_L, all using the legends from (g).

phases, as stress tends to concentrate more often in small local regions, making these areas more susceptible to damage. The relative total crack volume or area for mortar, $V_{ntf,m}$, ITZ, $S_{ntf,ITZ}$, and aggregate, $V_{ntf,a}$, are computed by summing relative cluster sizes. Their variations with respect to σ_L are provided in Fig. 8(d–f). To explicitly describe the variation of the PDFs with confining pressure and aggregate shape, the lognormal fitting, $f_{ln}(x_s)$, is applied to effectively capture the overall trend of the PDF, as below:

$$f_{ln}(x_s) = \frac{1}{x_s \sigma_s \sqrt{2\pi}} \exp\left(-\frac{(\ln x_s - \mu_s)^2}{2\sigma_s^2} \right) \qquad (28)$$

$$M = \exp\left(\mu_s + \frac{\sigma_s^2}{2} \right), \qquad (29)$$

where μ_s and σ_s are the fitting parameters of the lognormal fitting, x_s is the random variable for the PDF, which can be replaced by $V_{nf,m}$, $S_{nf,ITZ}$ and $V_{f,a}$. The analysis of the PDF based on this fitting uses Eq. (29) to

calculate its mean value, M, which can be replaced by M_m for mortar, M_{ITZ} for ITZ, and M_a for aggregate, as introduced in Fig. 8(g-i). This mean value of fitting is used to indicate the central tendency of the relative cluster size.

With increasing the confine pressure σ_L, the damage level in mortar, $V_{ntf,m}$, in Fig. 8(d) shows a nearly continuous decrease, whilst $S_{ntf,ITZ}$ and $V_{ntf,a}$ in Fig. 8(e) and (f), respectively, exhibit different trends in response to σ_L. We note that, compared to the uniaxial test, low confining pressures (e.g., 5 MPa) can even cause increases in damage levels in ITZ and aggregates, $S_{ntf,ITZ}$ and $V_{ntf,a}$, because the lateral constraint is insufficient to prevent fracture initiation or propagation in both material phases, driven by intensified overall stress. Nevertheless, confining pressure can restrict the growth direction of cracks, making them more likely to be confined to localised areas and resulting in smaller crack clusters, as evidenced by the reductions in M_{ITZ} and M_a in Fig. 8(h) and (i), respectively, in contrast to uniaxial test, where crack can freely develop. As σ_L increases beyond 5 MPa, damage levels in

mortar and aggregates, $V_{ntf,m}$ and $V_{ntf,a}$ in Fig. 8(d) and (f), respectively, progressively decrease. This is because the greater lateral constraint becomes more dominant, restraining deformation in the axial loading direction and potential shear failure. This significantly increases the strength required for material fracture, reducing the regions of experience severe damage. However, although the strength of the ITZ improves with higher σ_L, as described in the material model, it remains the weakest phase and is still the most susceptible to cracking. Therefore, $S_{ntf,ITZ}$ is not significantly inhibited for increasing level of confine pressure, as shown in Fig. 8(e).

Among all material phases, the mortar phase, $V_{ntf,m}$ and M_m as shown in Fig. 8(d) and (g), respectively, exhibits similar damage behaviour for different aggregate shapes, reflecting the universality of crack properties in mortar across varying confining pressures. The dependencies of $S_{ntf,ITZ}$ and $V_{ntf,a}$ on aggregate shapes are evident through their competition as F_d increases. Although the decrease in $V_{ntf,a}$ with increasing σ_L, as shown in Fig. 8(f), makes this competition less pronounced, it remains universal under varying confining pressures. This also indicates that higher level of stress concentration induced by rougher aggregates, whether in uniaxial tests or amplified in triaxial tests, persists during the post-peak regime and continues to promote the fracture propagation from the ITZ to aggregates. The mean of cracked region sizes, M_{ITZ} and M_a as shown in Fig. 8(h) and (i), respectively, exhibit no significant variation with increasing σ_L but still generally display universal competition between two material phases. This suggests that, in the case of rougher aggregates under confining pressures, cracking in the ITZ is constrained to propagate in smaller and more localised areas, leading to the more frequent formation of smaller clusters. When promoting fracture propagation into aggregates, higher stress concentration can also expand the fractured area within the aggregates, increasing the likelihood of forming larger crack clusters.

4. Conclusion

In this paper, the triaxial fracture behaviour of concrete, which contains aggregates with realistic shapes, is studied using mesoscale modelling based on the finite element method. The effect of aggregate shape on the macro strength of concrete under varying confining pressures is specifically investigated, with a focus on exploring the underlying microscopic information from the local response of concrete. These micromechanical features, such as distribution and evolution of stress, local damage, and crack clusters, are analysed to illustrate the universality observed in macroscopic mechanical responses.

Rougher aggregates lead to higher compressive strength of concrete, and this effect becomes more pronounced under higher confining pressure. The relation between confining pressure and normalised compressive strength for all aggregate shapes can be describe by the scaling law with only a single fitting parameter. It is found that the universal law in the triaxial loading regime relies on uniaxial responses, which are strongly dependent on the aggregate shape.

At the initial loading stage, rougher aggregates induce higher concentrated stress within the adjacent mortar phase, resulting in a significant difference in the heterogeneity of stress across samples with different aggregate shapes. As the loading increases toward compressive strength, this heterogeneity becomes universal across varying confining pressures. Confining pressure amplifies the stress concentration effects caused by rougher aggregates, further promoting fracture propagation from the ITZ into the aggregates and resulting in greater concrete strength. The competition among damage evolution in concrete phases across varying confining pressures allows the effects of aggregate shape on concrete strength to be reflected from triaxial to uniaxial tests and enables the scaling law to include the shape effects through normalisation while predicting concrete strength under confining pressure. The competition between the ITZ and aggregates also extends to crack and damage evolutions, illustrating that shape-induced stress concentration effects on fracture propagation from the ITZ to aggregates persist even in the post-peak regime. Under confining pressures, the competition in terms of crack clusters indicates that, for rougher aggregates, the ITZ tends to fracture into smaller clusters, while higher stress concentrations can expand the fractured zones within the aggregates, leading to larger fracture clusters.

In summary, the role of aggregate shapes on fracture behaviour of concrete under triaxial stresses has been comprehensively understood by examining local responses within the material phases. It provides a valuable insight for practical engineering applications, especially in concrete mixture design, where shape irregularity of aggregate associated with concrete strength and damage should be carefully considered. Our mesoscale model can be improved for future research to consider more complex multiaxial stress conditions, i.e., $\sigma_1 > \sigma_2 > \sigma_3$, as well as cases with mix-sized aggregates.

CRediT authorship contribution statement

Qingchen Liu: Writing – original draft, Visualization, Validation, Methodology, Investigation, Formal analysis, Data curation, Conceptualization. **Deheng Wei:** Writing – review & editing, Supervision, Software, Resources, Methodology, Investigation, Formal analysis, Data curation, Conceptualization. **Yixiang Gan:** Writing – review & editing, Visualization, Supervision, Resources, Methodology, Investigation, Funding acquisition, Formal analysis, Conceptualization.

Declaration of competing interest

The authors declare that they have no known competing financial interests or personal relationships that could have appeared to influence the work reported in this paper.

Data availability

Data will be made available on request.

References

[1] Ashby MF. Materials and the environment: eco-informed material choice. Elsevier; 2012.

[2] Sun M, Lv T, Zhang J. Upscaling coarse-grained simulation study for hydrated cement paste from mesoscale to microscale. Dev Built Environ 2024;17:100379.

[3] Pijaudier-Cabot G, Bažant ZP. Nonlocal damage theory. J Eng Mech 1987;113: 1512–33.

[4] Sun G, Poh L. Homogenization of intergranular fracture towards a transient gradient damage model. J Mech Phys Solids 2016;95:374–92.

[5] Garboczi E, Bentz D. Computational materials science of cement-based materials. MRS Bull 1993;18:50–4.

[6] Vandamme M, Ulm F-J. Nanogranular origin of concrete creep. Proc Natl Acad Sci 2009;106:10552–7.

[7] Garboczi EJ. Three-dimensional mathematical analysis of particle shape using X-ray tomography and spherical harmonics: application to aggregates used in concrete. Cem Concr Res 2002;32:1621–38.

[8] Zaitsev Y, Wittmann F. Simulation of crack propagation and failure of concrete. Mater Constr 1981;14:357–65.

[9] Kim S-M, Al-Rub RKA. Meso-scale computational modeling of the plastic-damage response of cementitious composites. Cem Concr Res 2011;41:339–58.

[10] Chen Q, Zhang J, Wang Z, Zhao T, Wang Z. A review of the interfacial transition zones in concrete: identification, physical characteristics, and mechanical properties. Eng Fract Mech 2024;109979.

[11] Wu Z, Zhang J, Fang Q, Yu H, Haiyan M. Mesoscopic modelling of concrete material under static and dynamic loadings: a review. Constr Build Mater 2021; 278:122419.

[12] Papanikolaou VK, Kappos AJ. Confinement-sensitive plasticity constitutive model for concrete in triaxial compression. Int J Solids Struct 2007;44:7021–48.

[13] Ouyang X, Wu Z, Shan B, Chen Q, Shi C. A critical review on compressive behavior and empirical constitutive models of concrete. Constr Build Mater 2022;323: 126572.

[14] Brown ET. Strength of models of rock with intermittent joints. J Soil Mech Found Div 1970;96:1935–49.

[15] Hoek E, Martin C. Fracture initiation and propagation in intact rock–a review. J Rock Mech Geotech Eng 2014;6:287–300.

[16] He Z-J, Zhang J-X. Strength characteristics and failure criterion of plain recycled aggregate concrete under triaxial stress states. Constr Build Mater 2014;54:354–62.

[17] Wang Y, Wu J, Ma D, Yang S, Yin Q, Feng Y. Effect of aggregate size distribution and confining pressure on mechanical property and microstructure of cemented gangue backfill materials. Adv Powder Technol 2022;33:103686.

[18] Bažant ZP, Tabbara MR, Kazemi MT, Pijaudier-Cabot G. Random particle model for fracture of aggregate or fiber composites. J Eng Mech 1990;116:1686–705.

[19] Schlangen E, Van Mier J. Simple lattice model for numerical simulation of fracture of concrete materials and structures. Mater Struct 1992;25:534–42.

[20] Zhai C, Herbold E, Hall S, Hurley R. Particle rotations and energy dissipation during mechanical compression of granular materials. J Mech Phys Solids 2019; 129:19–38.

[21] André D, Girardot J, Hubert C. A novel DEM approach for modeling brittle elastic media based on distinct lattice spring model. Comput Methods Appl Mech Eng 2019;350:100–22.

[22] Wei D, Hurley RC, Poh LH, Dias-da-Costa D, Gan Y. The role of particle morphology on concrete fracture behaviour: a meso-scale modelling approach. Cem Concr Res 2020;134:106096.

[23] Huang Y-J, Natarajan S, Zhang H, Guo F-Q, Xu S-L, Zeng C, Zheng Z-S. A CT image-driven computational framework for investigating complex 3D fracture in mesoscale concrete. Cem Concr Compos 2023;143:105270.

[24] Wang X, Zhang M, Jivkov AP. Computational technology for analysis of 3D meso-structure effects on damage and failure of concrete. Int J Solids Struct 2016;80: 310–33.

[25] Landis EN, Keane DT. X-ray microtomography. Mater Charact 2010;61:1305–16.

[26] Poinard C, Piotrowska E, Malecot Y, Daudeville L, Landis EN. Compression triaxial behavior of concrete: the role of the mesostructure by analysis of X-ray tomographic images. Eur J Environ Civ Eng 2012;16:s115–36.

[27] Zhang G, Torquato S. Precise algorithm to generate random sequential addition of hard hyperspheres at saturation. Phys Rev E: Stat Nonlinear Soft Matter Phys 2013; 88:053312.

[28] Tahmasebi P, Sahimi M, Kohanpur AH, Valocchi A. Pore-scale simulation of flow of CO2 and brine in reconstructed and actual 3D rock cores. J Pet Sci Eng 2017;155: 21–33.

[29] Stock A, Hannantt D, Williams R. The effect of aggregate concentration upon the strength and modulus of elasticity of concrete. Mag Concr Res 1979;31:225–34.

[30] Zhu S, Zhou Z, Xiong Y. Mesoscale fracture analysis of three-point bending concrete beams based on cohesive zone model. Eng Fract Mech 2024;296:109828.

[31] Zhou R, Lu Y, Wang W, Cheng C, Lu Z. Mesoscale modelling of the dynamic tensile strength of concrete in spalling tests using interface elements. Eng Fract Mech 2024;295:109808.

[32] Wu Y, Wang T, Duan J, Song L. Mesoscale numerical study of size effect on concrete fracture characteristics based on FDEM. Electron J Struct Eng 2025;25: 46–51.

[33] Ge L, Chen J-F. Meso-scale fracture analysis of concrete based on phase-field theory and cohesive zone method. Eng Fail Anal 2025;19:109684.

[34] Cai T, Zhang Z, Wang X, Yang Z, Zhou C, Li Y. A mesoscale approach for the three-dimensional modelling of interfacial debonding between FRP and concrete. Eng Struct 2025;327:119663.

[35] Naderi S, Tu W, Zhang M. Meso-scale modelling of compressive fracture in concrete with irregularly shaped aggregates. Cem Concr Res 2021;140:106317.

[36] Naderi S, Zhang M. Meso-scale modelling of static and dynamic tensile fracture of concrete accounting for real-shape aggregates. Cem Concr Compos 2021;116: 103889.

[37] Wang Q, Xu Y. Macro-meso cracking inversion modelling of three-point bending concrete beam with random aggregates using cohesive zone model. Theor Appl Fract Mech 2024;133:104566.

[38] Wu Z, She W, Zhang J, Tang J, Cao Y, Da B. 3D mesoscale modelling of steel fiber-reinforced aggregate concrete. Int J Mech Sci 2023;257:108550.

[39] Wu Z, Yu H, Zhang J, Ma H. Mesoscopic study of the mechanical properties of coral aggregate concrete under complex loads. Compos Struct 2023;308:116712.

[40] Pan G, Song T, Li P, Jia W, Deng Y. Review on finite element analysis of meso-structure model of concrete. J Mater Sci 2025;60:32–62.

[41] Wang J, Jivkov AP, Li Q, Engelberg DL. Experimental and numerical investigation of mortar and ITZ parameters in meso-scale models of concrete. Theor Appl Fract Mech 2020;109:102722.

[42] Wang J, Li X, Jivkov AP, Li Q, Engelberg DL. Interfacial transition zones in concrete meso-scale models–balancing physical realism and computational efficiency. Constr Build Mater 2021;293:123332.

[43] Chandrabhan S, Kumar GP. Biaxial behaviour of concrete and its failure mechanics under quasi-static and dynamic loading: a numerical study. Eng Fract Mech 2024; 300:109931.

[44] Ren Y, Chen J, Lu G. Mesoscopic simulation of uniaxial compression fracture of concrete via the nonlocal macro–meso-scale consistent damage model. Eng Fract Mech 2024;304:110148.

[45] Singh C, Gupta PK. Numerical analysis of failure mechanics of concrete under true dynamic triaxial loading using a four-phase meso-model. Constr Build Mater 2024; 450:138661.

[46] Ning Z, Li Y, Liu Y, Li Y, Dong J, Wang Q. A unified meso-scale simulation method for dynamic compressive and tensile properties of hydraulic asphalt concrete based on the viscoelastic damage contact model. Constr Build Mater 2025;484:141861.

[47] Zhang L, Xie H, Feng J. Effect of meso-structure on macroscopic behavior of concrete: a 3D numerical study. Arab J Sci Eng 2024:1–17.

[48] Wang J, Yu X, Fu Y, Zhou G. A 3D meso-scale model and numerical uniaxial compression tests on concrete with the consideration of the friction effect. Materials (Basel) 2024;17:1204.

[49] Wang L, Sun X, Xie L, Yu Z, Lian H, Lian Y, He H. Research on the shear multiaxial performance and meso-mechanical mechanism of concrete. Mater Struct 2025;58: 1–22.

[50] Yang L, Li K, Hu X, Peng Z, Liu Q-f, Shi C. Mesoscopic discrete modeling of compression and fracture behavior of concrete: effects of aggregate size distribution and interface transition zone. Cem Concr Compos 2024;147:105411.

[51] Maleki M, Rasoolan I, Khajehdezfuly A, Jivkov AP. On the effect of ITZ thickness in meso-scale models of concrete. Constr Build Mater 2020;258:119639.

[52] Wang B, Song X, Zhang Z. Mesoscopic fracture modelling of lightweight aggregate concrete under compression. Int J Comput Methods 2025;3:2441013.

[53] Huang Y, Yang Z, Ren W, Liu G, Zhang C. 3D meso-scale fracture modelling and validation of concrete based on in-situ X-ray Computed Tomography images using damage plasticity model. Int J Solids Struct 2015;67:340–52.

[54] Huang Y-J, Guo F-Q, Zhang H, Yang Z-J. An efficient computational framework for generating realistic 3D mesoscale concrete models using micro X-ray computed tomography images and dynamic physics engine. Cem Concr Compos 2022;126: 104347.

[55] Liu Q, Ma J, Qiao P, Wu E, Zhou G. Mesoscale modeling of new-to-old concrete interface under combined shear and compressive loads. Eng Fract Mech 2024;307: 110331.

[56] Ren Q, Pacheco J, de Brito J. Methods for the modelling of concrete mesostructures: a critical review. Constr Build Mater 2023;408:133570.

[57] Wei X, Sun Y, Gong H, Zhou Y, Hu M, Chen J. 2D aggregate gradation conversion framework integrated with 3D random aggregate method and machine-learning for asphalt concrete. J Mater Civ Eng 2024;36:04024091.

[58] Gao L, Zhou Y, Jiang J, Yang Y, Kong H. Mix-mode fracture behavior in asphalt concrete: asymmetric semi-circular bending testing and random aggregate generation-based modelling. Constr Build Mater 2024;438:137225.

[59] Wang B, Song X, Weng C, Yan X, Zhang Z. A hybrid method combining voronoi diagrams and the random walk algorithm for generating the mesostructure of concrete. Materials (Basel) 2024;17:4440.

[60] Zhang H, Xu C, Zhou Y, Shu J, Huang K. Hybrid phase-field modeling of mesoscopic failure in concrete combined with Fourier-Voronoi stochastic aggregate distribution modelling approach. Constr Build Mater 2023;394:132106.

[61] Liang Y, Chen H, Xu X, Xu Y, Xiao A. A comprehensive framework for 3D mesoscopic modelling of concrete: innovations in aggregate mixing, placement domain shapes, and aggregate volume fraction adaptability. Constr Build Mater 2025;472:140894.

[62] Su Y, Iyela PM, Zhu J, Chao X, Kang S, Long X. A Voronoi-based gaussian smoothing algorithm for efficiently generating RVEs of multi-phase composites with graded aggregates and random pores. Mater Des 2024;244:113159.

[63] Laubie H, Radjai F, Pellenq R, Ulm F-J. Stress transmission and failure in disordered porous media. Phys Rev Lett 2017;119:075501.

[64] Qin F, Hua ZJ. Three-dimensional numerical modelling of concrete-like materials subjected to dynamic loadings. Adv Prot Struct Res 2012;1:33.

[65] Mollon G, Zhao J. 3D generation of realistic granular samples based on random fields theory and Fourier shape descriptors. Comput Methods Appl Mech Eng 2014; 279:46–65.

[66] Liu Q, Cheng A, Sun C, Chen K, Wang Y, Li W. Effects of aggregate's type and orientation on stress concentration and crack propagation of modeled concrete applied a shear force. J Build Eng 2024;95:110340.

[67] Jin L, Liu K, Zhang R, Yu W, Du X. Effects of content and size of aggregate on the mechanical responses of concrete at cryogenic temperatures. Eng Fract Mech 2022; 273:108737.

[68] Jin L, Yu W, Li D, Du X. Numerical and theoretical investigation on the size effect of concrete compressive strength considering the maximum aggregate size. Int J Mech Sci 2021;192:106130.

[69] Zhang J, Emelianenko M, Du Q. Periodic centroidal voronoi tessellations. Int J Numer Anal Model 2012;9:950–69.

[70] Du Q, Faber V, Gunzburger M. Centroidal Voronoi tessellations: applications and algorithms. SIAM Rev 1999;41:637–76.

[71] Wei D, Wang J, Nie J, Zhou B. Generation of realistic sand particles with fractal nature using an improved spherical harmonic analysis. Comput Geotech 2018;104: 1–12.

[72] Chen P, Liu J, Cui X, Si SJC, Materials B. Mesoscale analysis of concrete under axial compression. Constr Build Mater 2022;337:127580.

[73] Zhou G, Xu Z. 3D mesoscale investigation on the compressive fracture of concrete with different aggregate shapes and interface transition zones. Constr Build Mater 2023;393:132111.

[74] Zhou R, Song Z, Lu Y. 3D mesoscale finite element modelling of concrete. Comput Struct 2017;192:96–113.

[75] D. Wei, R.C. Hurley, L.H. Poh, D. Dias-da-Costa, Y.J.C. Gan, C. Research, The role of particle morphology on concrete fracture behaviour: a meso-scale modelling approach. 2020;134:106096.

[76] Wei D, Wang Z, Pereira JM, Gan Y. Permeability of uniformly graded 3D printed granular media. Geophys Res Lett 2021;48.

[77] Wei D, Zhao B, Dias-da-Costa D, Gan Y. An FDEM study of particle breakage under rotational point loading. Eng Fract Mech 2019;212:221–37.

[78] Yankelevsky DZ. The uniaxial compressive strength of concrete: revisited. Mater Struct 2024;57:144.

[79] Zhang X, Wu H, Li J, Pi A, Huang F. Numerical simulation of high-strength concrete under uniaxial/triaxial compression based on meso-scale model. J Phys Conf Ser 2020;1507:082053.

[80] Chen H, Xu B, Mo Y, Zhou T. Behavior of meso-scale heterogeneous concrete under uniaxial tensile and compressive loadings. Constr Build Mater 2018;178:418–31.

[81] Xiong Q, Wang X, Jivkov AP. A 3D multi-phase meso-scale model for modelling coupling of damage and transport properties in concrete. Cem Concr Compos 2020; 109:103545.

[82] Yılmaz O, Molinari J-F. A mesoscale fracture model for concrete. Cem Concr Res 2017;97:84–94.

[83] Barenblatt GI. The mathematical theory of equilibrium cracks in brittle fracture. Adv Appl Mech 1962;7:55–129.

[84] Benzeggagh M, Kenane M. Measurement of mixed-mode delamination fracture toughness of unidirectional glass/epoxy composites with mixed-mode bending apparatus. Compos Sci Technol 1996;56:439–49.

[85] Lowes LN. Finite element modeling of reinforced-concrete beam-column bridge connections. Berkeley: University of California; 1999.

[86] Imran I, Pantazopoulou SJ. Experimental study of plain concrete under triaxial stress. ACI Mater J 1996;93:589–601.

[87] Sfer D, Carol I, Gettu R, Etse G. Study of the behavior of concrete under triaxial compression. J Eng Mech 2002;128:156–63.

[88] Mazzucco G, Pomaro B, Xotta G, Garbin E, Majorana C, De Marchi N, Concheri G. Meso-scale XCT-based modeling of ordinary concrete. Constr Build Mater 2021; 286:122850.

[89] Kotsovos MD, Newman JB. Mathematical description of deformational behavior of concrete under generalized stress beyond ultimate strength. Proc 1980:77.

[90] Candappa D, Sanjayan J, Setunge S. Complete triaxial stress-strain curves of high-strength concrete. J Mater Civ Eng 2001;13:209–15.

[91] Lu X, Hsu C-TT. Stress-strain relations of high-strength concrete under triaxial compression. J Mater Civ Eng 2007;19:261–8.

[92] Attard M, Setunge S. Stress-strain relationship of confined and unconfined concrete. Mater J 1996;93:432–42.

[93] Xie J, Elwi A, MacGregor J. Mechanical properties of three high-strength concretes containing silica fume. Mater J 1995;92:135–45.

[94] Chen Z, Hu Y, Li Q, Sun M, Lu P, Liu T. Behavior of concrete in water subjected to dynamic triaxial compression. J Eng Mech 2010;136:379–89.

[95] F.E. Richart, A. Brandtzæg, R.L. Brown, A study of the failure of concrete under combined compressive stresses. University of Illinois. Engineering Experiment Station. Bulletin; no. 185 1928.

[96] Sovják R, Vogel F, Beckmann B. Triaxial compressive strength of ultra high performance concrete. Acta Polytech 2013.

[97] Newman J. Concrete under complex stress. Dev Con Tech 1979;1:151–219.

[98] Binici B. An analytical model for stress–strain behavior of confined concrete. Eng Struct 2005;27:1040–51.

[99] Hsieh S-S, Ting E, Chen W. A plastic-fracture model for concrete. Int J Solids Struct 1982;18:181–97.